

Review

Beyond the First Tipping Points of Southern Hemisphere Climate

Terence J. O’Kane ^{1,*}, Jorgen S. Frederiksen ², Carsten S. Frederiksen ² and Illia Horenko ³

¹ CSIRO Environment, Battery Point, TAS 7004, Australia

² CSIRO Environment, Aspendale, VIC 3195, Australia; jorgen.frederiksen@csiro.au (J.S.F.); carsten.frederiksen@csiro.au (C.S.F.)

³ Faculty of Mathematics, Rhineland-Palatinate Technical University of Kaiserslautern-Landau, 67663 Kaiserslautern, Germany; horenko@mathematik.uni-kl.de

* Correspondence: terence.okane@csiro.au

Abstract: Analysis of observations, reanalysis, and model simulations, including those using machine learning methods specifically designed for regime identification, has revealed changes in aspects of the Southern Hemisphere (SH) circulation and Australian climate and extremes over the last half-century that indicate transitions to new states. In particular, our analysis shows a dramatic shift in the metastability of the SH climate that occurred in the late 1970s, associated with a large-scale regime transition in the SH atmospheric circulation, with systematic changes in the subtropical jet, blocking, zonal winds, and storm tracks. Analysis via nonstationary clustering reveals a regime shift coincident with a sharp transition to warmer oceanic sea surface temperatures and increased baroclinicity in the large scales of the Antarctic Circumpolar Circulation (ACC), extending across the whole hemisphere. At the same time, the background state of the tropical Pacific thermocline shoaled, leading to an increased likelihood of El Niño events. The SH climate shift in the late 1970s is the first hemispheric regime shift that can be directly attributed to anthropogenic climate change. These changes in dynamics are associated with additional regional tipping points, including reductions in mean and extreme rainfall in south-west Western Australia (SWWA) and streamflow into Perth dams, and also with increases in mean and extreme rainfall over northern Australia since the late 1970s. The drying of south-eastern Australia (SEA) occurred against a background of accelerating increases in average and extreme temperatures across the whole continent since the 1990s, implying further inflection points may have occurred. Analysis of climate model simulations capturing the essence of these observed shifts indicates that these systematic changes will continue into the late 21st century under high greenhouse gas emission scenarios. Here, we review two decades of work, revealing for the first time that tipping points characteristic of regime transitions are inferred to have already occurred in the SH climate system.

Keywords: climate change; atmospheric circulation; ocean circulation; storms; blocking; regimes; informatics



Citation: O’Kane, T.J.; Frederiksen, J.S.; Frederiksen, C.S.; Horenko, I. Beyond the First Tipping Points of Southern Hemisphere Climate. *Climate* **2024**, *12*, 81. <https://doi.org/10.3390/cli12060081>

Academic Editor: Timothy G. F. Kittel

Received: 20 March 2024

Revised: 24 May 2024

Accepted: 25 May 2024

Published: 31 May 2024



Copyright: © 2024 by the authors. Licensee MDPI, Basel, Switzerland. This article is an open access article distributed under the terms and conditions of the Creative Commons Attribution (CC BY) license (<https://creativecommons.org/licenses/by/4.0/>).

1. Introduction

The severe risk of potential tipping points in regional and global climate under global warming has been emphasized in a number of recent studies [1–4] and a recent report, *The Risks to Australia of a 3 °C Warmer World* (2021), by the Australian Academy of Science [5]. The aforementioned studies detail important regime transitions of the Earth system, which, if they were to occur, would be catastrophic, leading to a markedly less habitable future global climate. Interactions and reinforcements of regional tipping points, in particular, exceedance of warming thresholds, are already evident and impacting phenomena at high latitudes, including Greenland ice-sheet loss, Arctic sea-ice reduction, acceleration of Antarctic ice-sheet loss, and Siberian permafrost thawing [2]. Polar ice loss will inevitably lead to global impacts such as a rise in sea levels and has the potential to lead to a slowdown

of the Atlantic deep ocean circulation through freshwater injection. Additional regional impacts at lower latitudes are already evident in the die-off of coral reefs and increased frequency of droughts and forest fires.

There is evidence that changes in aspects of the Australian climate are sufficiently remarkable that regional regime transitions have already occurred [6]. Our purpose here is to review and collate the authors' and their collaborators' work describing hemispheric shifts in the Southern Hemisphere (SH) atmospheric and oceanic circulations and place the observed regional changes within the context of regime transitions in the background circulation. In doing so, we show that the inferred hemispheric circulation changes are dynamically consistent and are the primary causes of the regional regime transitions, indicating that hemispheric critical points have been exceeded. Moreover, projections based on skillful climate models indicate that the trends that have occurred during the 20th and early 21st centuries will continue into the late 21st century under high-emission scenarios. All of these results provide evidence that aspects of the SH climate system, and the Australian climate in particular, have transitioned beyond the first tipping points. The purpose here is to describe the manifestations of regime shifts in the atmosphere, ocean, and sea ice, as well as their changing dynamics and causes, as elucidated in observational and model data via nonstationary Granger causal [7,8] machine learning methods and instability calculations.

It is important to note that it is difficult to detect systematic spatio-temporal changes in the features of persistent coherent states under the influence of external covariates (radiative forcing) using analysis and/or machine learning methods where statistical stationarity is assumed. In such analysis, the underlying system's nonstationarity effectively reduces the sample size statistics that could be considered at least locally stationary, resulting in a classical "small data" problem. Parametric detrending, for example, via the application of a regression or spline, prior to applying popular machine learning tools, e.g., k-means clustering, neural networks, or EOF/PCA, to nonstationary data may lead to biased results since such time-series data can violate the underlying parameter stationarity assumption inherent in those common tools. For example, training a neural network on historical records results in obtaining fixed parameters, i.e., weights and biases, that are time-independent and do not change over the whole training interval. Where the neural network is trained on model simulations, the (climate) model biases are inherited by the machine learning process. As a consequence, such *parametric* tools have difficulties discerning nonstationary regime transitions between metastable states from relatively short and noisy observational data sequences [9–12].

To address the intrinsic nonstationarity, in the regime analyses presented here, we deploy a *nonparametric* nonstationary clustering methodology that has been shown to be successful in the analysis of high-dimensional time-series data with relatively short statistical lengths and high levels of noise across a broad class of problems, including molecular and fluid mechanics, geosciences, economics, and biomedicines. Specifically, we apply the nonparametric finite element–bounded variation–vector auto-regressive with external factors method (FEM-BV-VARX: [13–16]; also described in Appendix B) to nonstationary gridded climate reanalysis and simulation data. Complementary methods based on instability calculations and decomposition are further employed to better understand past changes in circulations and future trends.

Prior to the satellite era, we were limited to data products collected from the heterogeneous observational network available at the time. Observations from this early period were largely limited to in situ ocean measurements of temperature and salinity from shipping and moorings; land-based measurements of surface air temperatures, rainfall, and streamflows; and radiosonde and rawinsonde measurements of the atmosphere. In this way, reanalysis products contain larger uncertainties in their representations of atmospheric dynamics prior to the arrival of dense satellite observations. As satellite observations increased over time, sufficient spatial and temporal homogeneity was achieved to facilitate data assimilation systems with better constraints on model errors and, therefore, system-

atically reduced biases. This allowed for smaller assimilation increments and reduced uncertainties (spread) in the analyzed (reconstructed) states [17]. The degree to which one can assign an understanding of regime behavior in the climate system in the past is undoubtedly impacted by uncertainties in the observational network and biases in our climate model configurations. However, these uncertainties decrease at larger spatio-temporal scales, where a single sonde, for example, might be sufficient to characterize a large volume of the atmosphere. One of the advantages of reanalyses is that the data assimilation systems employed give important information on where and when uncertainties may be present [18,19]. The impact of additional data sources or a systematic change in the observing network over time can also impact the quality of reanalyses. For example, the introduction of Global Telecommunication System (GTS)-derived data in 1967 was seen to affect analysis fields for the high latitudes of the Southern Hemisphere [20,21]. While reanalysis products are not perfect, we argue that with the appropriate caveats and careful application, they offer the “best estimate” of the evolving dynamics of the climate system. In Appendix A, we provide a detailed discussion of the relative merits of reanalysis data for the SH prior to the satellite era and in particular for NCEP-NCAR reanalysis 1 (hereafter NNR1) [18,22]. In the present study, we not only examine reanalyses but also rely on purely observational products, model simulations, and theoretical arguments. Hence, it is on the preponderance of evidence that we rest our argument.

2. SH Atmospheric Circulation

Over the six decades between 1948 and 2009, systematic changes in the baroclinicity of the subtropical jets and their impact on regional precipitation trends over southern Australia occurred against a hemispheric regime transition in the large-scale flow. Specifically, large changes in SH storm track modes occurred in all seasons, including the austral winter, when blocking is at its most active [23]. The austral winter storm track changes manifest as reduced baroclinicity and a decrease in the July zonal winds of about 10 ms^{-1} in the subtropical jet relative to the earlier period 1949–1968 [24]. The changes in the storm track modes provide a dynamical mechanism for the observed systematic linear downward trends in the annual number of SH blocking events [15,25]. Such events predominantly occur in preferred locations about the Australian ($110\text{--}210^\circ \text{ E}$); eastern Pacific ($260\text{--}315^\circ \text{ E}$); and Indian ($20\text{--}80^\circ \text{ E}$) ocean sectors. These regions are associated with the ridges of the hemispheric wave-3 pattern [26,27], specifically the transition to a dominant Southern Annular Mode (SAM), i.e., the teleconnection pattern that characterizes a largely zonal state, and a weakening of the SH wavenumber 3 teleconnection pattern, which is associated with the three major regions of tropospheric blocking. Applying a data-driven methodology to atmospheric reanalyses, O’Kane et al. (2013) [15] first determined the time series of the prevalence of wavenumber 3 blocking states and the more zonal positive SAM states over recent decades. As summarized in Figure 1, they found systematic trends in the dynamics of the troposphere reflecting a marked decline in SH mid-latitude blocking (wave-3) during the post-1978 period accompanied by a strong trend to one biased toward the positive phase of the zonal SAM state, consistent with a more “summer-like” mid-latitude circulation [28,29]. In contrast, prior to the 1950s and 1960s, the flow was largely characterized by transitions between a dominant positive wave-3 teleconnection (enhanced blocking in the Tasman Sea and close to South Africa and Patagonia) and its sub-dominant negative phase (enhanced zonal flow in the Tasman Sea and close to South Africa and Patagonia). However, from late 1960, these preferred states underwent systematic changes, whereby the positive wave-3 state occurred less and less frequently as the westerly zonal jet intensified and moved poleward. During the same period, the negative wave-3 phase became increasingly zonal and more frequent, ultimately evolving into the dominant positive SAM phase associated with the increasingly strong polar jet stream westerlies observed in the most recent decades. These cluster results broadly agree with the changes in the zonal winds documented in the earlier instability calculations of Frederiksen and Frederiksen [24,30,31]. In particular, [24,31] showed that decreases in the subtropical jet

strength, reduced growth rates of mid-latitude blocks, and extratropical storms after the mid-1970s were coincident with the SAM being strongly correlated with increases in the polar jet strength. These results on the reduction in winter storm formation over Australia after the mid-1970s have also been confirmed in the data study in Osbrough and Frederiksen (2021).

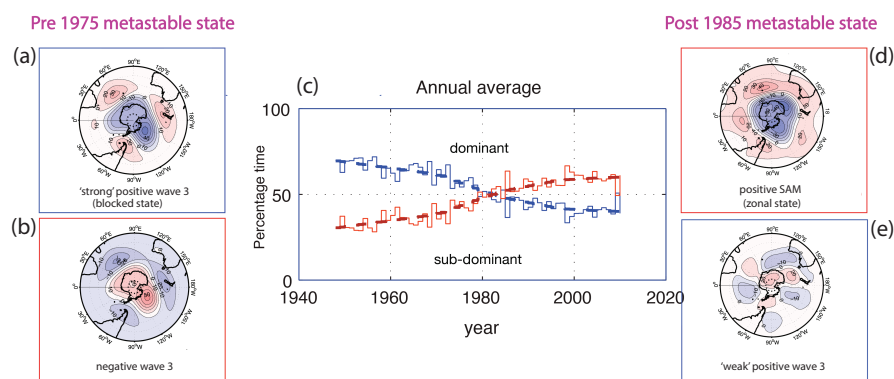


Figure 1. Regime states of 500 hPa geopotential height anomalies from the NNR1 data covering the period 1948–2009, averaged over all months of the year based on nonstationary data clustering (see Appendix B). The panels on the left show the spatial patterns of the persistent states of the SH mid-troposphere prior to the 1970s. In this period, the flow was largely characterized by transitions between (panel a) a dominant positive wave-3 blocking phase, i.e., enhanced blocking in the Tasman Sea and close to South Africa and Patagonia, and (panel b) its sub-dominant negative wave-3 zonal phase, i.e., enhanced zonal flow in the Tasman Sea and close to South Africa and Patagonia. Post-1980s, the negative wave-3 phase had transitioned into (panel d) the dominant zonal positive phase of the Southern Annular Mode (SAM), i.e., the teleconnection pattern that characterizes a largely zonal state. During the same period, the positive wave-3 blocking phase (panel a) significantly weakened in terms of amplitude, frequency of occurrence, and persistence to become subdominant (panel e) to the zonal positive SAM phase (panel d). Annual averages in the percentage of time spent in the respective metastable states (panel c) reveal systematic secular trends and a transition point in the early 1980s. Figure adapted from [15,28].

While an early study hypothesized that global warming is likely to change the frequency of occurrence of these circulation regimes but not their spatial patterns [32], the aforementioned studies reveal that the spatial character of the SH persistent climate regimes has indeed changed significantly during the period 1948–2009. As we discuss in detail in Section 2.2, Franzke et al. [28] subsequently conducted a formal attribution study to determine the relative role of anthropogenic greenhouse gas concentrations and other radiative forcing in driving the observed changes in the large-scale circulation of the SH troposphere. They found CO_2 , and to a lesser degree, the seasonal impact from stratospheric ozone, to be the dominant driver(s) of the observed systematic circulation changes. They also found that reduced temperatures associated with the emission of sulfate aerosols from particularly large volcanic eruptions allowed the positive wave-3 blocking state to temporarily re-establish as the dominant metastable state.

In the following sections, we examine the 1980s climate regime transition with a particular focus on the Pacific, where the impacts of the changed dynamics are most evident.

2.1. Sectorial Trends in the Frequency of Occurrence and Persistence of Synoptic Structures

O’Kane et al. (2013) [15] revealed evidence for significant secular trends in persistent circulation regimes associated with the SAM and a hemispheric wave-3 blocking pattern in all seasons. Subsequent examination by Franzke et al. (2015) [28] of the secular trends in the time spent in either a wave-3 blocked or zonal (positive SAM) state found that the observed increasing frequency and persistence of the positive SAM pattern is accompanied

by a corresponding decrease in the frequency and persistence of the wave-3 hemispheric pattern, which features blocking in the Australian, South American, and South African sectors. In an examination of JRA-55 reanalysis data [33], O’Kane et al. (2016) [29] reported that the hemispheric regime transition previously observed in NNR1 [22] also manifested in the late 1970s–early 1980s with similar correspondingly stronger zonal flows in the region to the south of the Australian mainland and a general reduction in baroclinic instability in the subtropics between 90° E and 180° E. A sectoral analysis further found that post-1980, over the western Indian Ocean and for the eastern Atlantic region to the east of South America, a significant reduction in baroclinic instability occurred, coinciding with a shift to more convergent upper-level winds. For the Australian–New Zealand sector between 150° W and 110° E, the summer periods were dominated by significant surface air temperature anomalies over the coast of Western Australia around Perth as a result of persistent anticyclones in this node of the circumpolar waveguide. The preferred wintertime state is characterized by warm surface air temperature (SAT) anomalies, upper-level divergence, strong baroclinic instabilities, and the generation of Rossby waves to the south of Perth and the southeast of Madagascar. A noticeable regime shift occurred in the summertime circulation around 1980 in the Pacific, where the summertime trends exhibited a transition from a period of relatively regular decadal variations between states to one characterized by a significant anticyclonic 500 hPa height anomaly to the south of the Tasman Sea, anomalously warm surface air temperatures extending from Tasmania to Victoria and then inland, and reduced baroclinic instability between the Australian mainland and 50° S. The annual trend indicates that the summertime circulation trends are dominant.

O’Kane et al. (2016, 2017) [29,34] showed that systematic changes in the persistence and frequency of occurrence of the formation and decay of coherent atmospheric states happen throughout all four seasons. However, the trend is nearly linear throughout the summer season, whereas a much more distinct regime transition occurs during the other three seasons.

2.2. The Transition to a Dominant Zonal Mean SAM⁺-like Circulation Post-1978

Climate models, traditionally the main method of investigating the role of radiative forcing in atmospheric circulation [35–40], have identified stratospheric ozone depletion as an important driver of the observed austral summertime intensification of the SAM over recent decades. However, stratospheric ozone depletion is a highly seasonal effect and plays no role in the austral winter–spring atmospheric circulation dynamics. The SH storm tracks are equally active all year round [41]. However, the austral wintertime is the season when the observed changes in the storm track activity, namely reduced blocking and baroclinicity of the subtropical jet [24], have been particularly evident, and they cannot be solely attributed to the ozone mass deficit (OMD). Franzke et al. (2015) [28] chose to examine Z^{500hPa} geopotential height anomalies (seasonal cycle subtracted) projected on the 20 leading EOFs and with the external covariates in a temporally regularized VARX model in terms of various combinations of the major radiative forcings. The forcings considered were the Cape Grim CO₂ measurements [42], sulfate aerosols [43], stratospheric aerosol optical thickness [44], solar constant [45], and stratospheric ozone mass deficit (OMD) [46], including accounting for the time-lagged seasonal OMD impacts on the circulation. They also considered the role of the major tropical internal modes of climate variability, specifically the ENSO (NINO 3.4) index, the Madden–Julian Oscillation (MJO) index, the Indian Ocean Dipole (IOD), and the eastern IOD mode indices. These indices describe tropical sea surface temperature (SST) variability (ENSO, IOD) or an intrinsic mode of tropical intraseasonal variability (MJO).

Deploying the FEM-BV-VARX method, comprehensive sensitivity tests were carried out [28] for the cluster parameters involving memory depths between 0 and 5 days, where 2 days were found to be optimal, and several choices of annealing steps between 4 and 64. Daily forcing agents were spline-interpolated with no lag apart from the OMD, and

every possible combination of forcing agents was considered, including the observed OMD lagged by 0, 30, 60, and 90 days, as well as a variant with a lag average spanning 365 days. The optimal external radiative forcing agent was ultimately found to correspond to the Cape Grim CO₂ time series determined by the application of the Akaike Information Criteria (AIC) [47]. This is equivalent to assuming that the scalar-valued squared model errors are χ^2 distributed and that the vector-valued FEM-BV-VARX model errors are Gaussian. The analysis found strong evidence that anthropogenic greenhouse gas concentrations are the root cause of the observed secular trends in the SAM and hemispheric wave-3 pattern. The clustering analysis with CO₂ forcing found a corresponding Akaike weight of close to 1, denoting the most parsimonious explanation for the observational data among all other fitted explanatory statistical models, with all possible combinations of radiative forcings considered and taking into account possible overfitting.

The associated metastable states and their features were seen to have very different expressions and corresponding surface air temperature (SAT) signatures. The wave-3 blocked regime dominant prior to the late 1970s climate transition corresponded to a cold SAT anomaly over the Antarctic Peninsula and warm SAT anomalies over the Ross Ice Shelf, the coast of Antarctica's Victoria land, and over South America. The zonal positive SAM regime was associated with a warm SAT anomaly over East Antarctica and Australia and a cold SAT anomaly along the coast of Antarctica's Wilkes Land. An examination of the trend in SAT for the same period (1979–2010) calculated from yearly averaged Had4Krig version 2.0.0 data [48], showed remarkable agreement between the dominant SAM state SAT anomaly pattern and the Had4Krig SAT trend pattern over Antarctica, providing further independent evidence of the weakening of the wave-3 blocking state. The strong trend toward the SAM state in recent decades coincides with recent reports of the loss of Antarctic ice mass.

The results in Franzke et al. (2015) [28] are in contrast to earlier studies, which indicated a much more dominant role of O₃ [37,46,49]. In particular, the study by Roscoe and Haigh (2007) [46] suggested that ozone depletion (OD) is up to nine times more important than anthropogenic CO₂ concentrations in explaining these trends. Their study considered only 365-day lagged OD, where the ozone is considered to act in all seasons. The aforementioned study mainly focused on the austral summer season and the poleward shift of the Hadley Cell, increasing westerly winds, and the linear trend in the zonal mean circulation toward the positive SAM phase. They focused on changes in the mean state rather than the frequency of occurrence and structural changes of the synoptic features in the data. Freitas et al. (2015) [50] demonstrated that these interdecadal changes in the SH circulation could, in fact, be simulated with a general circulation model forced by observed SSTs and historical time-varying CO₂ concentrations. Importantly, the FEM-BV-VARX data-driven methodology represents a nonstationary extension of Granger causal inference [7] applied to attribute changes in the entire SH circulation, including time-evolving systematic changes in the frequency and persistence of coherent synoptic features, to all possible combinations of the relevant radiative forcings.

2.3. Weakening of the Subtropical Jet and Storm Tracks and Impact on Rainfall over Southern Australia

Australian, particularly south-west Western Australian (SWWA), rainfall and associated streamflows are affected by circulation features, including the Indian Ocean Dipole (IOD: [51]), SAM [35,52]), to some extent the Southern Oscillation Index (SOI: [53]), and to a lesser extent various other indices, including local effects such as land clearing [15,29,34,54–59]. Frederiksen and Frederiksen (2007,2005) [24,30] found that large-scale atmospheric circulation phenomena and associated changes in extratropical storms were major factors in the SWWA rainfall reductions post-1970s. Importantly, the large-scale atmospheric zonal wind changes were seen to extend around the whole SH in patterns dominated by a longitudinally symmetric component. The aforementioned studies focused on changes in the atmospheric circulation and storm tracks in terms of differences between two periods, namely (1975–1994) and

(1949–1968). They showed that in the latter period, the average peak zonal wind in July in the subtropical jet between 30° S and 35° S, as well as between 100° E and 130° E, decreased by 9.4 ms⁻¹ or 17% at 150 hPa, representing a substantial drop in the strength of the thermodynamical engine driving the SH circulation, which was reflected in a circa 20% reduction in SWWA rainfall at the time. These largely zonally symmetric wind changes were further associated with a reduction in the temperature gradient between the high and middle latitudes, an increase in the average SAM index, and a related increase in the strength of the polar jet.

Another particularly important aspect of the changes in atmospheric circulation before and after the mid-1970s has been the reduction in the potential for storm formation due to a weakening of the subtropical jet. Frederiksen & Frederiksen (2007) [24] analyzed the Phillips instability criterion [60] for SH storm development. This criterion measures the vertical shear of the zonal wind relative to a critical threshold shear, calculated based on winds at 300 hPa, 700 hPa, and the critical value, $u^{300} - u^{700} - u^{critical} > 0$, which is necessary for instability leading to storm formation. Here, $u^{critical}$ depends on the vertical temperature gradient and the Coriolis parameter, which remained essentially constant between the two periods. Based on reductions in baroclinicity, they showed (Figure 2 in the aforementioned work) that one would expect a reduction in storm formation in the latitude band 25° to 35° S at practically all longitudes in the SH and an increase further south. They showed that the changes in the Phillips criterion for storm formation were consistent with more complex instability calculations of the growth and structures of extratropical storms affecting southern Australia. These calculations revealed that the growth rates of fast-growing storms were reduced by as much as 30% in the period post-1975 compared with the earlier period. In addition, some storms were deflected southward.

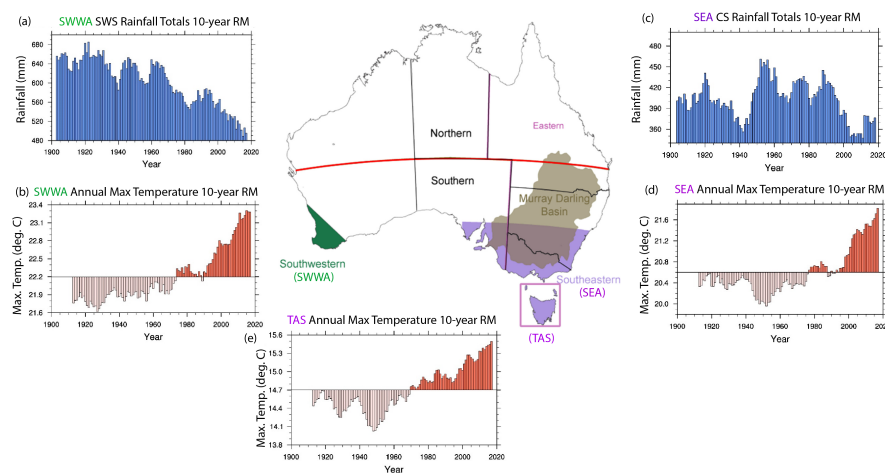


Figure 2. Through to the late 1970s, a consistent weakening of the upper-troposphere jet occurred poleward of 30° S, with a maximum reduction at circa 150 hPa, combined with strengthening further south and corresponding broad-scale changes in the zonal wind difference between 300 hPa and 700 hPa. These pronounced circulation changes, including reduced storm track activity, were accompanied by temperature increases and rainfall decreases over south-west Western Australia (SWWA) and south-eastern Australia (SEA) from the mid-to-late 20th century. Panels (a,c) reveal these changes through the 10-year running mean (RM) of SWWA during the Southern Wet Season (SWS) and SEA rainfall totals for the Cool Season (CS) from April to October. Panels (b,d,e) show the 10-year running mean of the SWWA, SEA, and Tasmanian (TAS) annual maximum temperatures, respectively. Figure adapted from [6].

Frederiksen and Frederiksen (2011) [31] later documented additional changes in the major large-scale atmospheric circulation anomalies associated with changes in unstable weather modes during the 10-year interval from 1997 to 2006 at the start of the Australian Mega-Drought (AMD). Specifically, they performed comprehensive model-based instability

studies of the three-dimensional circulation, finding that the reduction in baroclinicity, particularly in the Australian region of the subtropical jet, resulted in reductions in the growth rate of leading storm track modes (of more than 30%) and onset-of-blocking modes (around 20%) but increases in the growth of north-west cloud band (NWCB) modes [61] and intraseasonal oscillation activity (Table 2 of [31]). In an observational study of the synoptic components of rainfall variability in SEA, Risbey et al. (2013) [62] found that during the AMD, the reduction in rainfall was due to fewer intense fast-growing frontal storms and cut-off lows associated with the reduced baroclinicity in the subtropical jet in the Australian region, consistent with theoretical predictions [24,31]. Compared to a baseline period from 1949 to 1968, the zonal wind in a longitudinal belt around 30° S was reduced by as much as 8 ms⁻¹ at 300 hPa and increased by similar amounts near 55° S, whereas at 700 hPa, the corresponding changes in magnitudes were as large as 5 ms⁻¹ or more. These differences were again shown to have a zonally symmetric component but with significant peaks around the longitudes of the Australian continent. Latitude height cross-sections of the zonal wind averaged between 110° E and 160° E showed a peak reduction of more than 6 ms⁻¹ near 150 hPa at 30° S and a slightly large increase peaking near 250 hPa at 55° S. Consistent anomalies occurred in the 500 hPa temperature, as well as in the geopotential height and sea level pressure (Figure 3 of [31]).

The changes in the hemispheric circulation and extratropical storms before and after the mid-1970s, as described for the peak austral winter season, are reflected by broadly similar changes in other seasons. Frederiksen et al. (2017) [40] revealed systematic changes in all seasons over the second half of the twentieth century in terms of changes in the annual cycle of SH baroclinic instability. They showed significant negative trends in baroclinic instability, as measured by the Phillips Criterion, in the regions of the climatological storm tracks, occurring against significant positive trends in a zonal band occurring further poleward. These changes were accompanied by corresponding changes in the growth rate of storm formation at these latitudes during this period, with a general preference for storm formation to be moved further poleward than had previously been the case. The weakening of the upper-troposphere jet just poleward of 30° S, with a maximum reduction at circa 150 hPa and strengthening further south, corresponded to a general decline until the late 1970s, followed by annual variability, but no systematic trend was observed thereafter. These broad-scale features were also seen in the zonal wind difference between 300 hPa and 700 hPa, as well as in temperature increases accompanied by rainfall decline (see Figure 2) over south-eastern Australia from the mid-to-late 20th century [6,31,40].

3. Pacific and Southern Hemisphere Oceans

We now focus on observed widespread and systematic shifts that occurred simultaneously across the SH oceans, with a particular focus on ocean teleconnections between the tropical Pacific Ocean and higher latitudes. We examine the dynamic and thermodynamic internal ocean pathways and the atmospheric processes that excite these modes to form oceanic bridges connecting the tropical Pacific to the higher latitudes.

3.1. ENSO Teleconnections

Freitas et al. (2015) [50] first showed that the tropospheric circulation changes described in Section 2 were coincident with a shift to warmer sea surface temperatures (SSTs) in the southern oceans. In this section, we examine the evidence for tropical–extratropical oceanic teleconnections, the role of ENSO, and the mechanisms by which atmospheric forcing drives this shift.

In the tropics, preceding a period of strong and sustained El Niño events during the late 1970s, the equatorial Pacific thermocline basic (time mean) state shoaled, becoming more El Niño-like. O’Kane et al. (2014) [63] described the two distinct equatorial regimes as follows:

- Regime 1 (prior to 1978): A deepened western equatorial Pacific thermocline basic state and a more stably stratified (weakly stratified) density structure below (above) the thermocline.
- Regime 2 (post-1978): A shallow western equatorial Pacific thermocline basic state and a more stably stratified (weakly stratified) density structure above (below) the thermocline.

The upper panel (b) in Figure 3 depicts the observed ENSO variability (Multivariate ENSO Index (red line) and Niño3.4 Index (blue line) from HadISST data compared to that simulated by a coupled ocean–sea-ice model forced with bulk formulas derived from the NNR1 (black line). A regime state with generally smaller and cooler anomalies existed prior to the 1980s, whose mean thermocline state, shown in the left panel insert, is given by the vertical gradient of temperature. The Hovmöller diagram (lower panel b) of sea surface height anomalies between 15° N and 52.5° S and averaged over longitudes spanning the Pacific shows a transition from predominantly negative anomalies with corresponding cooler surface temperatures prior to 1980 between 15° S and 52.5° S, with maximum values around 30° S.

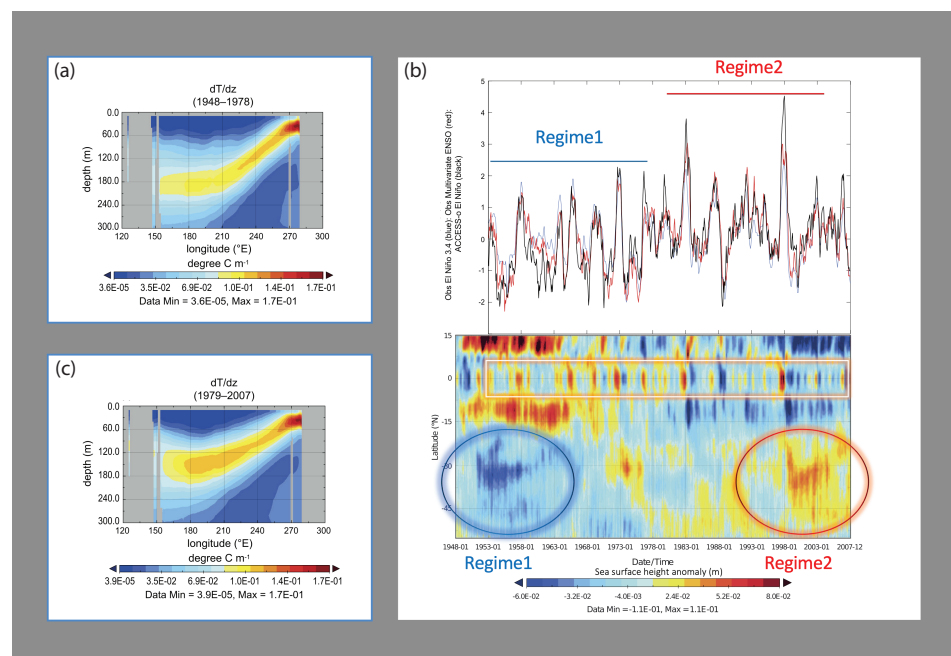


Figure 3. (a) The mean thermocline position (derivative of temperature with respect to depth) for the years 1948–1978 and (c) 1978–2007. (b upper) Comparison of the observed ENSO variability (Multivariate ENSO Index (red) and Niño3.4 Index (blue)) with the model Niño3.4 (black)). (b lower) Hovmöller plot of sea surface height anomaly (time versus latitudes 15° N–52.5° S), averaged over longitudes spanning the Pacific. ENSO variability at the equator is indicated by the yellow box. Panel (a) shows the equatorial Pacific thermocline in the early period before the transition to a new regime post-1978 depicted in panel (c), where the ocean thermocline basic state became consistently shallower and more “El Niño-like”. In panel (b), the observed and simulated time series of ENSO post-1980 reveals increased El Niño amplitudes relative to the earlier period. The increased intensity of ENSO post-1980 is also reflected in the sea surface height anomalies shown in panel (b lower), where we also see that in the subtropics and mid-latitude Pacific, a new regime emerged post-1980, dominated by positive height anomalies associated with a warmer surface ocean and seen in a sustained shift to warmer upper ocean temperatures in the region [70–22.5° S, 120 E–60° W] associated with the South Pacific decadal oscillation (SPDO). Here 1E-01 corresponds to 1×10^{-1} . Figure adapted from [63,64].

Between 1975 and 1983, the ocean underwent a transition to a new regime, where the ocean thermocline basic state was shoaled with respect to the earlier period (panel c), and a number of very strong El Niño events occurred. Evident in the time series of ENSO is an enhanced low-frequency component post-1980. In the subtropics and mid-latitude

Pacific, a new regime emerged, dominated by positive height anomalies associated with a warmer surface ocean and seen in a sustained shift to warmer upper ocean temperatures (5 m to 280 m) in the region 70–22.5° S, 120 E–60° W associated with the South Pacific decadal oscillation (SPDO). Using a linear inverse model framework, Lou et al. (2020) [65] showed reconstructions of the low-frequency SPDO variability in both observations and simulations (Figure 3), with correlations between the reconstructed SPDO and the observed or simulated SPDO of 0.81 and 0.73, respectively. They found that upper-ocean temperature anomalies in the mid-latitudes also exhibited low-frequency regime behavior of the type associated with the 1980 regime transition. The systematic changes to a more “El Niño-like” equatorial ocean thermocline and increased amplitude of El Niño variability also coincided with a similar shift in the variability and phase of the Interdecadal Pacific Oscillation (IPO) (Figure 4) [66].

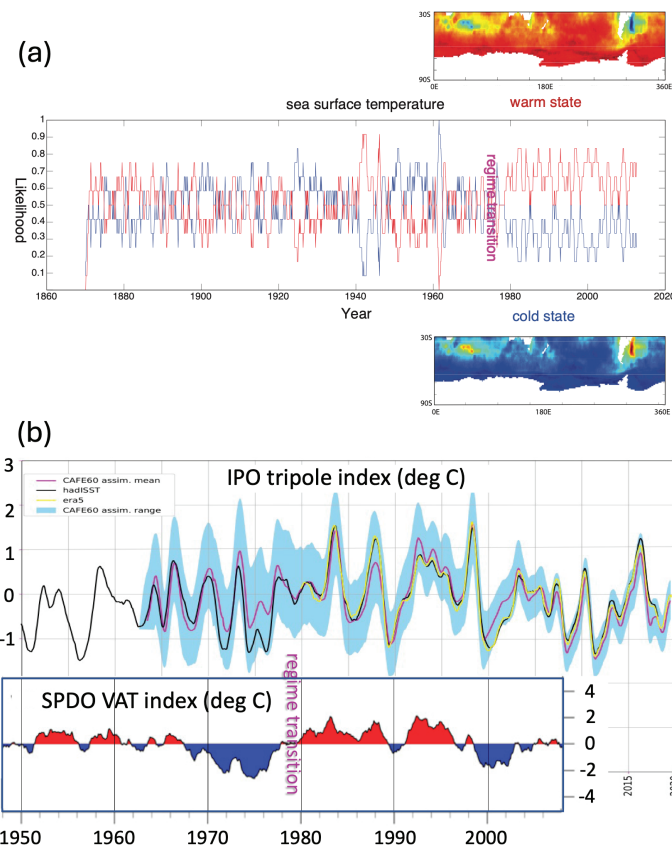


Figure 4. (a) Composite regime states of SST anomalies based on the FEM-BV-VARX cluster analysis (see Appendix B) of HADISST data over the region south of 30° S. Values greater than 0.1 or less than −0.1 are significant at the 95 % confidence level. (center-right panel) Time series of the model affiliation sequence $\gamma_i(t)$ from the cluster analysis of HADISST data with a 12-month digital filter applied. The blue (red) line corresponds to cold state 1 (warm state 2). (b) Time series of the Interdecadal Pacific Oscillation from HadISST, ERA5, and the CAFE60 large ensemble reanalysis, which includes uncertainty estimates in terms of the ensemble spread, calculated from an O(100) member ensemble Kalman filter. Subsurface South Pacific Decadal Ocean variability via vertically averaged temperature (SPDO VAT) over the upper 300 m in the South Pacific 70–22.5° S, 120° E–60° W). Figure adapted from [50,65,66].

Applying nonstationary cluster analysis [67], Freitas et al. (2015) [50] examined Pacific Ocean SSTs during the period between January 1870 and August 2012 from HadISST data. Retaining only the first 10 components from an EOF/PCA decomposition, the two leading cluster states (Figure 4) reveal warm and cold persistent anomalous states relative to the background state. The warm state 2 corresponds to large-scale warming of the southern

ocean with enhanced warming of the western boundary currents—the East Australian Current, Brazil–Malvinas Confluence, and the Agulhas Current. In this case, for any given data instance (monthly mean), the clustering finds the state that is most similar to the data, assigning probabilities $\gamma_i(t)$ (Equations (A2)–(A6)) indicating the likelihood that the data are in a given metastable state. Subsequently, a binary classification of the data associates the monthly mean HADISST data with one of either the warm or cold metastable regimes. Averaging the anomalies according to $\gamma_i(t)$ shows the broad features, whereas the application of a 12-month digital filter to the affiliation sequence reveals trends in the data. We see that prior to about 1978, there was marked switching between states interspersed with periods of relative persistence in a given state but with no discernable preference for one state over the other. Post-1978, the system was locked into a warm state.

3.2. South Pacific Ocean Teleconnections

In the remaining sections, we show how dynamical teleconnections internal to the ocean also bear the imprint of the 1980 tipping point. We begin by describing one of the longest continuous records of SSTs in the SH, namely the time series at Maria Island just east of Tasmania, the imprint of the 1980 tipping point, and the mechanism through which the observed variability arises. In Figure 5, we show the “ocean storm tracks” that allow large-scale baroclinically unstable waves to transverse the South Pacific subtropics within waveguides associated with potential density gradients at latitudes and depths associated with mode water formation. The pathways and mechanisms through which coherent baroclinically unstable disturbances propagate, are trapped, and amplified via resonant interaction with topography can be summarized from the findings in [68] as follows:

- The potential energy of the large-scale mean ocean circulation is generated by the action of the large-scale mean wind field.
- This energy is converted from baroclinic (APE) to barotropic (EKE) energy in regions where subtropical mode water forms.
- The associated baroclinic disturbances are inherently nonlinear and multiscale, and they are amplified and/or trapped through resonant interaction with topography.
- These nonlinearly modified Rossby waves are associated with persistent states that develop after the eddy wave number spectrum becomes saturated and long-wavelength coherent structures form.

These wavelike features provide an important mechanism to communicate information about interannual time scales across the Pacific, Indian, and mid-latitude oceans [68,69].

In Figure 5, we show a schematic describing the aforementioned waves and their pathway across the South Pacific to the east coast of Australia, where they enter the East Australian Current (EAC) via the South Caledonian jet and South Equatorial Current [70]. Having entered the EAC, these disturbances can amplify and then traverse the EAC and its extension toward Maria Island or traverse the Tasman Front from near Sydney toward New Zealand. The figure panel depicting the Maria Island station SST time-series data (4-year running mean) shows increasingly larger amplitudes in the low-frequency variability post-1980. The models, including data assimilation, all display the observed variability. The assimilation models incorporate subsurface temperature (T), salinity (S), and satellite SST data. All model variants shown are able to simulate the observed variability at Maria Island, with data assimilation acting to remove systematic biases rather than impose variability. At the location of Maria Island, the model maximum of the thermocline potential temperature gradient $d\theta/dz$, the buoyancy frequency N^2 , and the baroclinic energy conversion Φ' , here normalized, scaled, and a 4-year running mean applied, are all significantly correlated with the observed SST variability (p -value < 0.05). Notably, the baroclinic energy conversion, relating the energy transfer from the mean horizontal density gradients to the transients, undergoes a major increase in amplitude post-1980. Sloyan and O’Kane (2015) [70] postulated that the strong correlations between the simulated and reanalyzed ocean data and the observed SST at Maria Island suggest that the variability is strongly connected to the stability of the thermocline. They examined transport anomalies

entering the East Australian Current at the Australian boundary and exiting via either the Tasman Front or the EAC extension. This examination showed that periods of anomalously strong EAC transport at 25° S correspond to an anomalously strong Tasman Front and anomalously weak EAC extension (see Figures 15 and 16 of [70]) and weaker stratification (N^2), smaller thermocline temperature gradients, and energy conversion, with peaks in SST variability at Maria Island (see Figure 17 of [70]) Conversely, anomalously weaker EAC transport at 25° S corresponds to an anomalously weaker Tasman Front and an anomalously stronger EAC extension and stratification (N^2), larger thermocline temperature gradients, and increased energy conversion. Taken together, their results show that Maria Island SST variability is fundamentally linked to baroclinic stability in the Tasman Sea, which, in turn, is linked to the stability of the larger South Pacific Ocean. In particular, the dramatic change in the stability of the EAC post-1980 is seen to have a clear influence on the region's thermocline structure and on the component EAC currents and their associated transports.

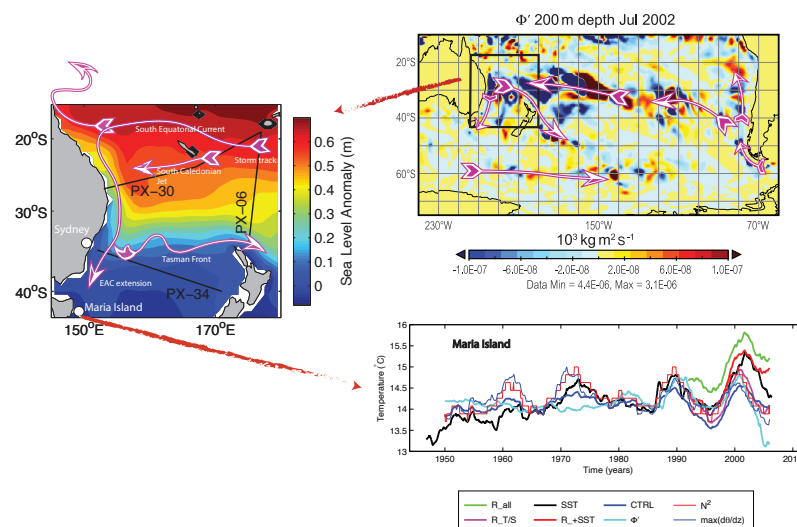


Figure 5. (left panel) Mean sea level anomaly (color) from the CTRL model (1950–2007), showing the location of XBT lines and a schematic of major currents. (top right) Pathways for the propagation of baroclinic Rossby wave disturbances across the Pacific to the south equatorial current to the EAC, influencing the temperature variability of the Tasman front and at Maria Island. These disturbances are confined within waveguides determined by potential density gradients and are the oceanic equivalent of storm tracks in the atmosphere. (bottom right) Temperature (°C) time series of the Maria Island station from in situ observations (SST) and a free-running model forced with reanalyzed winds (CTRL); assimilating subsurface temperature and salinity profiles (R_T/S); including satellite sea surface temperatures (R_+SST); and incorporating satellite sea surface height observations (R_ALL). In the control simulation (CTRL), no data are assimilated to constrain the ocean model; however, the model still incorporates surface fluxes derived from atmospheric reanalyses (NNR1), providing some constraint in the boundary conditions. To facilitate comparison with models that have assimilated ocean observations, a 1.8° SST bias has been subtracted from the CTRL simulation at Maria Island. Φ' represents the mean to transient potential energy conversion averaged over 150–350 m depth; N^2 denotes the Brunt–Vaisala (buoyancy) frequency averaged over 0–350 m depth; and $\max(d\theta/dz)$ indicates the maximum of the vertical derivative of temperature describing thermocline variability. N^2 and $\max(d\theta/dz)$ are derived from the CTRL simulation and are normalized and scaled for comparison to the observed SST variability (black line). Here 1E-01 corresponds to 1×10^{-1} . Figure adapted from [68,70].

4. The Stability of the High-Latitude Southern Oceans and Sea Ice

O'Kane et al. (2013) [64] identified the Southern Ocean near the East Pacific Rise to be a key region where low-frequency intrinsic variability arises largely due to topographic–baroclinic processes. Their simulations also described a nonlinear relationship between

atmospheric forcing, thermocline ocean disturbances, and sea-ice variability. Large-scale coherent wave-trains of potential energy occur coincident with significant density gradients becoming topographically trapped in the region of the East Pacific Rise. In this region, both baroclinic and barotropic instabilities are largest during the mature phase of regimes due to the combined effects of surface forcing related to the SAM, ENSO, and fast synoptic-scale disturbances.

They showed how noise-induced intrinsic variability may be amplified by either the low-frequency SAM (zonal variations) and/or ENSO (latitudinal variations) modes of variability, and that it is the Pacific sector of the Antarctic Circumpolar Current (ACC) where large-scale intrinsic variability manifests most readily. They also found that high-frequency winds (HFREQ) can further act to excite a significant internal ocean response in the Pacific, although weaker than that excited by either the SAM or ENSO modes. Both the zonal SAM and HFREQ weather modes are able to generate wave-like anomalies in the SH mid-latitude oceans capable of propagation from the Pacific to the Atlantic sectors, thereby establishing an oceanic teleconnection. However, only the weather modes were found to be capable of significantly amplifying those disturbances upon reaching the Atlantic sector.

Importantly for the discussion here, O’Kane et al. (2013) [64] found that the low-frequency variability observed in model simulations could be explained in terms of dynamical regimes. By applying the FEM-BV-VARX method to the three-dimensional ocean once again, the time series of regime affiliations was shown to have the frequency of atmospheric forcing embedded in it, along with trends in the time spent in each particular regime state. A pivot point indicating a fundamental change in the dynamics of the ocean–ice system was found to occur in the mid-1980s. The statistically significant trends observed in these component-forcing experiments again reflect the marked decline in atmospheric SH mid-latitude blocking during the post-1978 period, accompanied by the trend toward a more prevalent positive SAM phase [15]. The authors showed that both the intrinsic and forced decadal modes of variability in the ACC could be associated with dynamical regimes that respond to systematic changes, not only in the dynamically relevant climate modes (SAM and ENSO) but also in response to systematic changes in the synoptic weather patterns. The SH mid-latitude oceans were shown to undergo a regime change lagging behind that of the SH mid-latitude atmosphere by about 5 years (Figure 6). Further examination of a suite of experiments combining various components of the atmospheric forcing showed that this delay was mostly attributable to a lagged response due to the influence of ENSO at high latitudes. In Figure 6, three composite states arising from forcing with bulk formulas derived from NNR1 reanalysis (CORE2) show large variability in the Pacific around 150–110° W. State 1 is largely unstructured, while states 2 and 3 have a similar pattern but with opposite signs. The most coherent response in the Atlantic sector occurs in states 2 and 3, with maxima/minima in the vicinity of 60° S 15° E. Coherent large-scale structures also appear in the Pacific sector of the ACC, but there are features throughout the entire circumpolar domain. The composites show that the unstable region of intrinsic variability in the South Pacific is related to the South Atlantic Weak Mode (SAWM) region of the ACC, exhibiting complex three-state regime behavior. Obvious trends are observed toward state 2 and away from states 1 and 3. Prior to 1980, all states generally exhibited few or no trends in the duration of time spent in each state. The percentage of time spent in any given state largely reflects the fact that between 1978 and 1988, there was a pivot point where the relative dominance of each dynamical regime state changed. The SAM and HFREQ pivot points occurred almost coincidentally with the 1970s atmospheric regime transition, whereas the ENSO transition lagged by about 7–10 years. The pivot point for the ocean regime transition occurred around 1984, trailing the atmosphere by about 5 years.

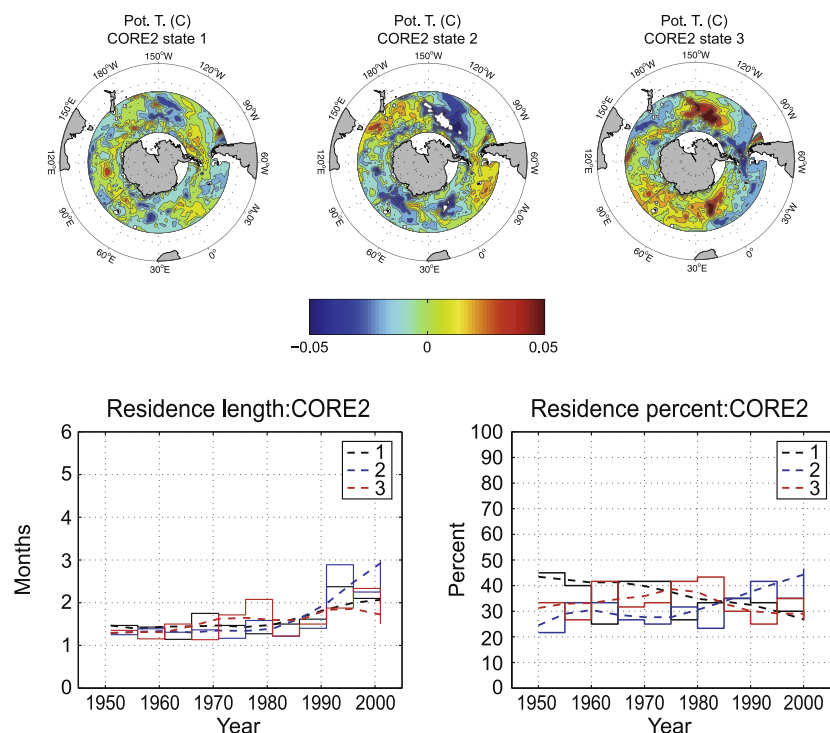


Figure 6. (Upper panels) FEM-BV-VARX cluster states at T200 dbars. The analysis revealed three composite states arising from forcing the coupled ocean–ice model with bulk formulas derived from NNR1 (CORE2). (Lower panels) Duration spent in each state (left panel) and percentage of time (right panel) spent in any given cluster state. The dashed lines are LOESS smoothed fits to the time-averaged data. The values and averaging periods of the time-averaged data are represented by the solid lines. Figure adapted from O’Kane et al. (2013) [64].

The mechanisms through which ENSO variability affects the higher latitudes remain somewhat controversial. However, all theories involve the influence of the Pacific South American mode [71]. Recently, it has been proposed that thermal wind affects ENSO variability, influencing the leading PSA mode (PSA1) [71] and that the combination of this mode and stochastic resonance induced by fast synoptic-scale processes (PSA2) induces a reddened response in the South Pacific [72], forming an effective oceanic bridge between the tropics and extra-tropics.

Regime behavior was further observed in sea-ice formation around Antarctica. In Figure 7, we show the leading two EOFs and PCs of ice concentration for various forcing combinations. Intrinsic variability generated by nominal year forcing plus small-scale noise (CORE1 (1a and b)) reveals little variability outside of the Pacific. Given that the CORE1 atmospheric forcing [73] has a significant noise component, it has been concluded that sea-ice variability is more closely coupled to weather systems in this region. SAM variability (2a and b), associated with the zonal westerly winds, enhances sea-ice variability in the Ross and Weddell seas but most noticeably introduces sea-ice variability throughout the entire circumpolar region. Meridionally oriented latitudinal variations due to the PSA and ENSO (3a and b) induce a more coherent larger-scale response in the Pacific, amplifying the underlying intrinsic variability but only yielding a marginal response in the Atlantic sector. Weather forcing (HFREQ not shown) induces coherent regions of large-scale variability in both the Pacific and Atlantic regions of the Southern Ocean. The response to full interannual forcing (CORE2) can be reproduced using a linear combination of the aforementioned component responses. The CORE2 simulation regime affiliations show a clear transition between two dominant and one neutral regime states (Figure 6), with the regime transition also reflected in at least one of the leading principal component (PC) time series for all of the forced sea-ice simulations (Figure 7).

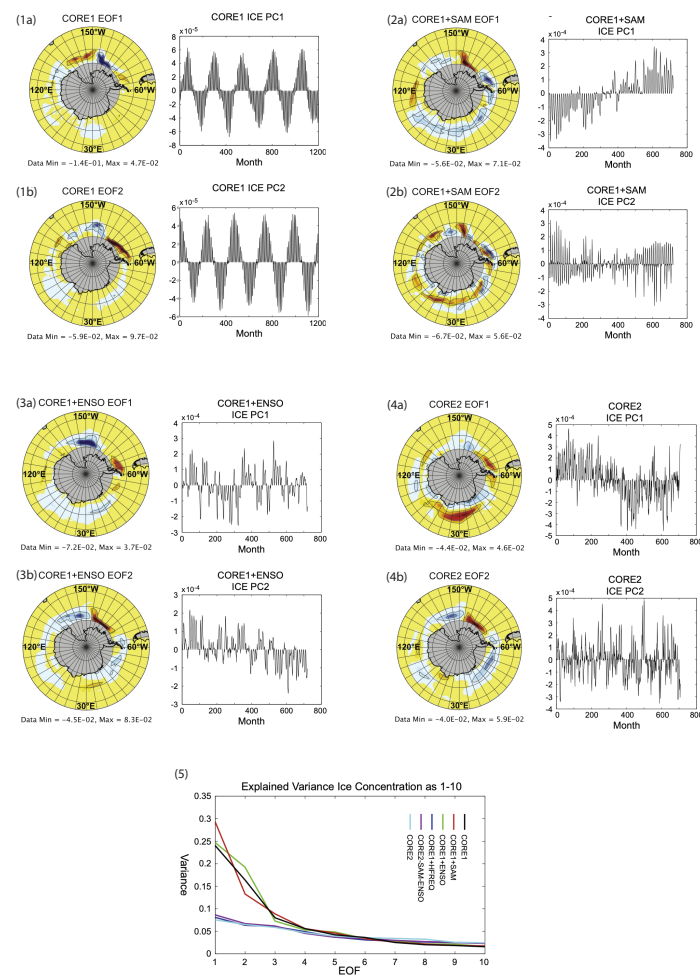


Figure 7. The leading 2 PCs of sea-ice concentration for various forcing combinations. These are nominal year atmospheric (CORE1); nominal year + southern annual mode (CORE1 + SAM); nominal year + ENSO (CORE1 + ENSO); nominal year + synoptic variability (CORE1 + HFREQ); and observed atmosphere (CORE2). The CORE1 PC1 timeseries (panel 1a right) and PC2 timeseries (panel 1b right) exhibit decadal oscillations with a 20-year period that modulates the annual sea-ice cycle. CORE1 + SAM PC1 (panel 2a,2b) shows a distinct increasing trend that matches the observed SAM trend present in the reanalyzed CORE2 dataset. CORE1 + ENSO PC1 (panel 3a right) and PC2 (panel 3b right) shows a distinct correlated with latitudinal variations in the atmospheric forcing. CORE1 + HFREQ PCs (not shown) display large-scale low-frequency sea-ice variability coincident with the unstable regions of the subsurface ocean. The leading CORE2 PC1 (4a right) and PC2 (4b right) exhibit a less easily interpretable response, with no clear relationship to the leading thermocline PCs, and they cannot simply be regarded as a linear combination of the constituent component experiments. Panel (5) shows the explained variances as a percentage of the total for the leading 10 EOFs for ice concentration. The CORE1 + SAM, CORE1 + ENSO, and CORE1 (intrinsic) component forcing experiments have steep slopes over the first 3 modes. Here $1\text{E}-01$ corresponds to 1×10^{-1} . Figure adapted from [64].

5. Spiciness Pathway

South Pacific subtropical density compensated temperature and salinity anomalies are known to be associated with equatorial thermocline variability. Disturbances generated in the eastern subtropics are advected toward the central equatorial Pacific Ocean, where they can directly modulate the thermocline [63,74,75]. Munk (1981) [76] first introduced

the term “spiciness” to describe differences in the temperature (T) and salinity (S) of water of a given density on a given isopycnal surface. Tailleux et al. (2005) [77] formulated a general theory for such disturbances, through which equatorward propagating subsducted salinity anomalies amplify while their temperature counterparts are attenuated. To first order, spiciness anomalies are both pressure and density compensated, so they are advected passively in the thermocline mean circulation from the eastern subtropics toward the tropics. It has now been recognized that the late 1970s transition to warmer tropical conditions [78] coincided with the arrival of a large-scale, subsurface cold and fresh water anomaly in the central tropical Pacific [63]. By developing an ocean reanalysis for the period from 1990 to 2007 that assimilated subsurface Argo, XBT, and CTD data, O’Kane et al. (2014) [63] showed that these anomalies occurred due to the subduction of negative surface salinity anomalies from near 30° S, 100° W, and were advected along the $\sigma = 25 - 26 \text{ kg m}^{-3}$ isopycnal surfaces. Taking about seven years to reach the central equatorial Pacific, they may have substantially perturbed the thermocline before breaking up, where the remnants of salinity ultimately ventilated in the region of the western Pacific warm pool. Spicy (warm and salty) disturbances occurred due to late winter diapycnal mixing and isopycnal outcropping, leading to the subduction of subtropical mode waters and subsurface injection. On reaching the equatorial band (10–0° S), these disturbances tended to deepen the thermocline, reducing the likelihood of large El Niño events occurring. In contrast, the emergence of negative (cold–fresh) disturbances at the equator, has been associated with a shoaling of the thermocline and El Niño events. This spiciness pathway is described in Figure 8.

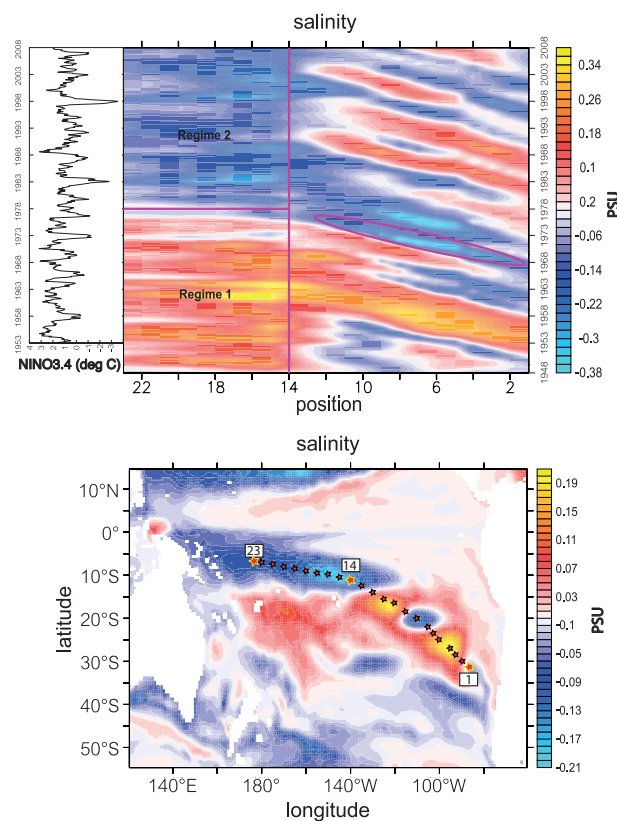


Figure 8. (upper panel) Hovmöller diagrams for the propagation of salinity anomalies across the Pacific Ocean, traversing the subtropical latitudes near the coast of South America to the western equatorial region along the positions indicated in the lower panel. The trajectory of the 240 m salinity anomaly corresponding to the shoaling of the thermocline is indicated by the ellipse. The NINO3.4 index calculated from HadISST data is shown in the left panel insert. (lower panel) 240 m salinity (psu) anomalies on 1 January 1990. Red stars indicate the location of the positions indicated in the Hovmöller plot. Figure adapted from [63].

We can now augment our previous discussion of the tropical Pacific thermocline regimes and SST variability in the following way:

- Regime 1 (prior to 1978): A deepened western equatorial Pacific thermocline basic state and a more stably stratified (weakly stratified) density structure below (above) the thermocline. This is further associated with a warm–salty (cold–fresh) anomaly structure below (above) the thermocline.
- Regime 2 (post-1978): A shallow western equatorial Pacific thermocline basic state and a more stably stratified (weakly stratified) density structure above (below) the thermocline. This is further associated with a cold–fresh (warm–salty) anomaly structure below (above) the thermocline.

6. Projections of the Future SH Climate

Coupled ocean–atmosphere–sea-ice models are our primary tool for understanding the future climate and hence the lifetime of a given climatic regime. In order to have confidence in simulations of the future climate, i.e., projections, it is important that climate models can realistically simulate the large-scale teleconnections over the historical record, including the climatological storm tracks, during the twentieth century. While it is not reasonable to expect climate models to capture the observed occurrences and phases of specific teleconnections, e.g., El Niño, we do expect that they are, at the very least, able to accurately simulate the trends and variance of those teleconnections, if not the observed causal relationships [79]. Frederiksen and colleagues tested the ability of successive programs of climate model development in simulating the observed austral winter changes in climatological baroclinicity, including the storm tracks from CMIP3 [80] through to CMIP5 [40]. They found that most models simulated the changes in zonal wind, but only about a third of the models captured the observed changes in baroclinic instability with reduced magnitude. The subset of models capable of simulating the observed spatial trends in the Phillips Criterion and the associated changes in winter rainfall over southern Australia, especially in SWWA, were used as a basis for a subsequent CMIP5 multi-model ensemble study conducted by Grainger et al. (2017) [81]. They found that the externally forced austral summer (DJF) variability in the Z^{500hPa} geopotential height resided almost exclusively in an SAM-like teleconnection with uniform positive loading in the tropics, extending to at least 30° S, exhibiting an annular structure with negative loadings at higher latitudes. In the austral winter (JJA), they showed a similar teleconnection that displaced more equatorward, with the largest annular loadings over southern Australasia, especially over SWWA, consistent with a reduction in the zonal westerly wind near 30° S and an observed reduction in baroclinity over the region. In both seasons, the slow external modes of variability were found to have a positive trend over the second half of the twentieth century, reflecting the projected thermal expansion of the tropical troposphere and a poleward shift of the downward branch of the Hadley Cell.

Grainger et al. (2017) [81] further showed that for SWWA, the negative trend in rainfall was closely associated with the aforementioned annular pattern in Z^{500hPa} geopotential height, with positive height anomalies and anti-cyclonic flow at 300 hPa over the region of decreasing rainfall. Frederiksen and Grainger (2015) [58] had earlier identified this same pattern in the leading slow external geopotential height mode of covariability in multi-model ensemble CMIP3 simulations and attributed this trend to external radiative forcing, including greenhouse gases. An analysis over the last 50 years of the twenty-first century in the RCP8.5 scenario [40] (Figure 9) showed a similar slow external mode of covariability but with an increasing downward trend in rainfall and an upward trend in the positive height anomaly over SWWA, together with a much stronger anti-cyclonic circulation in the winds at 300 hPa.

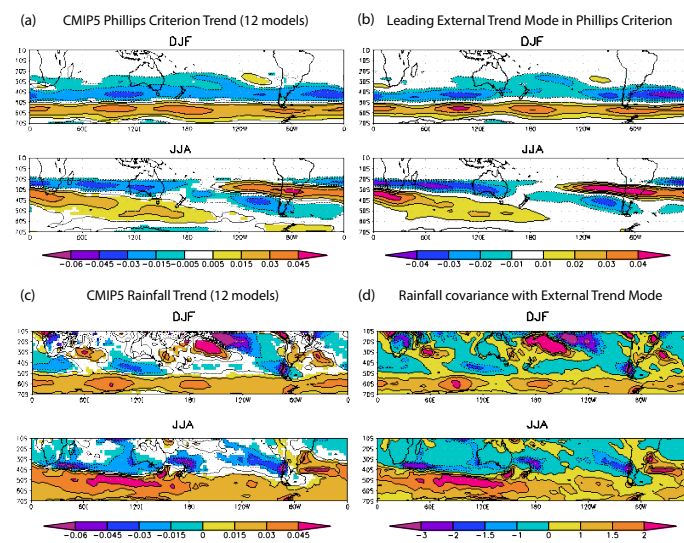


Figure 9. CMIP5 multi-model ensemble (2050–2099) trends in the SH. (a) Phillips Criterion ($\text{ms}^{-1} \text{year}^{-1}$) and (c) rainfall ($\text{mm day}^{-1} \text{year}^{-1}$), along with the covariance between the external components of the (b) Phillips Criterion and (d) rainfall, and the associated time series of the leading external trend mode. Significant trends at the 95% confidence level or greater are shaded. Figure adapted from [40].

In Figure 9, the trends in RCP8.5 CMIP5 model projections are shown for the Phillips Criterion and rainfall, along with the corresponding leading external modes for the austral summer and winter. Statistically significant trends $>99.9\%$ confidence levels were found for the leading external mode in each season (DJF 0.90 , JJA $0.85 \text{ ms}^{-1} \text{year}^{-1}$, respectively), with increased variance of the leading external mode shown to be substantially larger than for simulations with observed historical radiative forcings. Frederiksen et al. (2017) [40] argued that the close similarity between the pattern of the projected trends and the horizontal structure of the external trend mode, with pattern correlations in DJF and JJA of 0.98 in each season, respectively, are an indication that the external forcing determines the trends in baroclinic instability, and hence rainfall, largely due to anthropogenic greenhouse gases. A similar analysis with the RCP4.5 scenario, which exhibits a pathway to stabilization over the last 50 years, showed a near-complete collapse of this slow externally forced mode of covariability, indicating the importance of the continuing increase in greenhouse gas forcing.

7. Summary and Conclusions

Identifying, let alone understanding, regime behavior in the broader climate system is clearly a considerable challenge. The challenges occur not simply because of the multiple timescales involved but due to the requirement that the observational network be continuous and of sufficient homogeneity in space and time across all of the domains of the system. Efficiently diagnosing regime behavior requires not only observations and model simulations but also appropriate diagnostic tools for decomposing high-dimensional, nonstationary, and multiscale data. Here, we have employed nonstationary temporally regularized clustering for regime identification alongside energetics and instability calculations, as well as more standard methods of dimension reduction and decomposition, such as singular spectral analysis, EOF/PCA, and vector auto-regressive methods. The importance of applying analysis and modeling systems appropriate to the task cannot be underestimated.

Given the paucity of observations of the subsurface ocean prior to the advent of the Argo program [82], we must rely on model simulations to characterize the subsurface ocean before about 2001 (see Figures 1 and 2 in [17]). Where an ocean model can, in part,

be constrained by surface forcing from atmospheric reanalysis, significant secular trends have been observed in the states of the South Pacific, Southern Ocean, and sea ice around Antarctica since the 1950s. Here, we have seen that systematic and rapid shifts in either the large-scale components of the atmospheric circulation (SAM, ENSO) or changes in the frequency and persistence of synoptic-scale features in atmospheric variability alone can initiate a regime change in SSTs, thermocline variability, oceanic baroclinic instability (i.e., Rossby wave activity), sea-ice variability, and spiciness disturbances. We have seen that tropical variability (ENSO) is communicated to the high latitudes by the atmosphere, leading to a reddened oceanic response, and that there exist dynamic oceanic pathways that feedback this response to, in turn, modify the background regime.

In combination, these studies show the complexity of the climate system and its response to changes across domains. In particular, they detail the dynamic oceanic response to systematic changes in the coherent structures of the troposphere via coherence resonance effects. These responses include impacts on sea-ice variability and the energetics of the Southern Ocean. Positive reinforcement and feedback between the domains of the Earth system are now manifest in the poleward shift of the tropospheric westerly winds, further enhanced via changes in meridional temperature gradients induced by a pronounced shift to warmer SSTs.

We propose that the SH climate system underwent a systematic regime shift in the late 1970s and early 1980s. Attribution studies of observational and reanalysis data [83] clearly show that this shift first occurred in the atmosphere, primarily due to increasing rates of CO₂ exacerbated by seasonal O₃ mass deficit. The shift in tropospheric dynamics to a more SAM-like summer circulation coincided with increased surface air temperatures, reduced storm formation, and rainfall over southern Australia. The ocean responded with increasing thermocline, SST, and baroclinic variability and instability in the EAC and generally warmer SSTs throughout the South Pacific. The imprint of the climate regime shift can even be seen in the high-latitude upper-ocean and sea-ice variability. Analysis of CMIP historical and projection simulations [40,58], consistent with the attribution study by [28], points to CO₂ emissions as the dominant driver of the late 1970s regime transition. Without substantial reductions in CO₂ emissions, the current regime dominated by an *SAM-like* zonal state, a weakened subtropical jet, and expanded tropics will persist into the foreseeable future. These findings are summarized in Table 1.

The relative paucity of observations in the SH has exacerbated the difficulty of first identifying and fully understanding this climate tipping point. It is only now, nearly 40 years after the transition, that we can fully appreciate the impacts on the South Pacific and its surroundings. If one were to consider similar changes in the mid-latitudes of the Northern Hemisphere, with comparable consequences for long-term rainfall and temperatures, then one could imagine that enormous pressure would be placed on human systems. A final note of caution regarding CMIP projections relates to the huge uncertainties associated with the response of the Antarctic ice sheets and SH cryosphere to the circulation regime we now find ourselves in. Currently, CMIP models do not have dynamic cryosphere model components, and the relatively short observational record limits our understanding of even the natural variability of Antarctic glaciers and ocean–ice shelf interactions [84]. More broadly, given the difficulties in simulating the temporal variability of the ocean-driven seasonal to interannual modes, i.e., MJO, IOD, and ENSO, with follow-on impacts for our ability to simulate teleconnections to the atmosphere, it is arguable that we are dramatically and systematically underestimating near-term climate risks and overestimating our ability to simulate regime transitions of the scale presented. In this regard, there is a great need for advances in the methods of interrogating high-dimensional, multiscale, nonstationary data to better identify biases in climate teleconnections and inform the development of the next generation of climate models.

Table 1. Summary of the major findings.

Mid-latitude SH troposphere
<ul style="list-style-type: none"> • In the mid-1970s there was an expansion of the Hadley Cell and a poleward shift of the subtropical and polar jet streams. • This was accompanied by a reduction in the strength of the subtropical jet and an increase in the polar jet. • There was also a strengthening of the Southern Annular Mode, a systematic weakening of the hemispheric wave-3 pattern associated with the major blocking regions, and increased mid-latitude atmospheric temperatures between the two jet streams as required by thermal wind balance. • This, in turn, resulted in reduced (explosive) cyclogenesis and reduced frontal rainfall near the subtropical jet and increases near the polar jet, with dramatic effects on Southern Australia, particularly declines in SWWA rainfall and streamflows. • These systematic changes in circulation were followed by increasing surface temperatures over Australia.
SH low-latitude and equatorial regions
<ul style="list-style-type: none"> • Post-1980, the basic state of the western equatorial Pacific thermocline flattened (shoaled) and preconditioned for the generation of a series of large amplitude El Niño events that occurred during the 1980s–2010s. • The transition to a shoaled thermocline was coincident with the emergence of cold–fresh disturbances at the equator associated with late winter diapycnal mixing and isopycnal outcropping leading to subduction of subtropical mode waters and subsurface injection off western South America.
SH subtropics and southern oceans
<ul style="list-style-type: none"> • In the subtropics and mid-latitude Pacific, a new regime emerged post-1980 dominated by positive height anomalies associated with a warmer surface ocean. • This hemispheric shift to sustained warmer upper-ocean temperatures was also associated with the South Pacific Decadal Oscillation. • The shift in the large-scale structure of the atmosphere impacted the potential density gradients of the South Pacific subtropical oceans, which act as waveguides for the propagation of baroclinically unstable disturbances that teleconnect regions across the entire Pacific and are reflected in the observed long-term temperature record at Maria Island.
SH high latitudes
<ul style="list-style-type: none"> • Systematic changes in the synoptic variability of the mid-troposphere are communicated to subsurface disturbances in the Southern Ocean via coherence resonance and are reflected in their persistence and frequency of occurrence. • Trends in sea-ice variability and spatial heterogeneity are highly influenced by long-term trends in the SAM and the interannual variability of ENSO, but in certain regions, they are dominated by secular trends in synoptic variability.
The future SH climate
<ul style="list-style-type: none"> • Climate models were able to simulate the observed changes in zonal winds, but less successfully the observed austral seasonal changes in climatological baroclinicity and the storm tracks. • Climate projections indicate that external forcing due to anthropogenic greenhouse gases determines the trends in circulation and baroclinic instability and strongly influences rainfall, particularly over SWWA. • Projections of the future climate by more reliable climate models showed that greenhouse gas forcing produced a continuation of the trends in changing jet streams, baroclinicity, and rainfall, including reductions over Southern Australia in each season. • Projections with more reliable climate models showed that increasing greenhouse gas forcing of mid-tropospheric variability imposed an SAM-like teleconnection. • The slow external modes of variability were found to have a positive trend over the second half of the twentieth century, reflecting the projected thermal expansion of the tropical troposphere and a poleward shift of the downward branch of the Hadley Cell. • Under climate projections with a stabilization of the anthropogenic greenhouse gases, the trends seen in circulation and rainfall largely dissipate.

Author Contributions: Conceptualization, T.J.O. and J.S.F.; methodology, T.J.O., J.S.F., C.S.F., and I.H.; software, T.J.O., J.S.F., C.S.F., and I.H.; validation, T.J.O., J.S.F., C.S.F., and I.H.; formal analysis, T.J.O., J.S.F., C.S.F., and I.H.; investigation, T.J.O., J.S.F., C.S.F., and I.H.; resources, T.J.O., J.S.F., C.S.F., and I.H.; data curation, T.J.O., J.S.F., C.S.F., and I.H.; writing—original draft preparation, T.J.O.; writing—review and editing, T.J.O., J.S.F., C.S.F., and I.H.; visualization, T.J.O., J.S.F., C.S.F., and I.H.; supervision, T.J.O.; project administration, T.J.O.; funding acquisition, T.J.O., J.S.F., C.S.F., and I.H. All authors have read and agreed to the published version of the manuscript.

Funding: This research received no external funding.

Data Availability Statement: No new data was generated nor used in the course of this review.

Acknowledgments: T.J.O., J.S.F., and C.S.F. acknowledge the support of the CSIRO.

Conflicts of Interest: The authors declare no conflicts of interest.

Appendix A. On the Reliability of Reanalysis in the Pre-Satellite Period

Due to the paucity of satellite observations prior to 1979, the question arises as to whether the mid-tropospheric regime shift is robust or occurs as a data artifact due to the assimilation of insufficient observations to constrain model errors in constructing the reanalyses. To address this concern, we make the following points:

- Much of the work on SH atmospheric circulation changes has focused on their relationship to rainfall in the Australian sector. This is the region with the earliest and increasingly largest rawinsonde network in the SH, long before 1979. The earliest was established in 1942 at station 44021 Charlesville Aerodrome and was rapidly expanded in 1950, with 35 stations operational at least a decade prior to the satellite era. The Australian Bureau of Meteorology currently launches 20,000 balloons per year from 44 stations. In short, there should be no doubt that there were sufficient data over Australia (and New Zealand) to constrain the troposphere in the NNR1 in the pre-satellite era.
- As discussed, we have found broad agreement between the reanalysis products (NNR1 and JRA55). While [6] discussed their preference for NNR1 data in the earlier periods, O’Kane et al (2016) [29] found similar trends in blocking and the variability of persistent synoptic-scale structures in JRA55 to those reported by Wiedenmann et al. (2002) [25]. Harries and O’Kane (2021) [79] showed that even the causal relationships between the various climate teleconnections are robust across NNR1 and JRA55.
- Hertzog et al. (2004) [85] noted the superiority of the first variant of the NCEP reanalysis (NN50) relative to ERA40 for the early period from 1957 to 1979. Concerning the EOLE experiment at the end of the pre-satellite period, they reported that *the results presented ... are likely representative of the whole 1957–1979 period as the upper-air SH observation network was almost frozen during that period, and that the EOLE balloons drifted in the upper troposphere and lower stratosphere ... notice the good coverage of the SH between 20° S and 70° S. On their p. 8, they noted that ERA40 has also difficulty in reproducing the zonal-velocity peak at 40° S, whereas from 1967, NN50 and subsequently NNR1 assimilated the first satellite-derived cloud winds ... with sufficient quality and sampling rate to estimate atmospheric winds from cloud motions.* They argued that NNR1 performs better, exhibiting a more zonally symmetric response to change and superior performance, including over Antarctica (see Figure 8 of [85]).
- Bromwich et al. (2004) [86] noted that NNR1 assimilated a larger and more diverse set of observations prior to the satellite period and that *a more detailed look at the pre-satellite era reveals many shortcomings in ERA-40, particularly in the austral winter.* Similarly, Figure 6 of [86] shows high and quite consistent correlations with observations at 500 hPa and since 1958 at the three Antarctic stations—Scott, Casey, and Halley—with much better correlations between 1958 and 1975 than for ERA40. Regarding NNR1, they further noted that (Figure 7 on p. 4616 of [86]) *The time series at Perth have little systematic error for the whole period from 1958.* Much of the improved performance in NNR1 during the pre-1975 period is due to a reliance on station observational networks rather than a reliance on sparse satellite data. Figure 6e,f of [86] show that ERA40 remains inferior to NNR1 in terms of the RMSE for 500 hPa geopotential height comparisons during the 1960s.
- Most concerns about the reliability of reanalysis products in the SH have not been related to the continents but to the oceans, and in particular, south of 45° S. Hines et al. (2000) [20] noted that *extreme weather phenomena and sharp topographic contrasts also create unique difficulties for Antarctica.* They further noted that *... more than 20 radiosonde stations over Antarctica ... began operating in the 1950s or early 1960s. Thus, a sufficient number of stations appear to have been in place to reasonably establish the climatological pressure field near the Antarctic coastline from the late 1950s to the present.* Bromwich et al.

(2004) [86] noted that examining reanalyses at the 500 hPa height *has the benefit of being the first mandatory pressure level that lies fully above the high Antarctic interior*, thus avoiding most of the complexities at the surface discussed by [20]. Indeed, [20] also noted that *Some upper-air observations were incorporated into the NNR1 reanalysis during the 1950s and 1960s*. It is interesting to note from Figure 3 of [20] that around the time of the International Geophysical Year (1957), the upper-air average observations between 75–60° S and 45–180° W are comparable to those in the 1970s, and this signal is not seen in the surface observation data. Our regime analysis has been entirely focused on the mid-troposphere, not the surface.

- The work in Marshall (2003) [21] concerned an SAM index (BAS SAM) based on surface pressure, thereby encountering the full complexities of the steep topographic gradients and surface storms discussed in point 2. In particular, the analysis in [87] suffered from interpolation-extrapolation of the NNR1 reanalysis to the coast of Antarctica. Consequently, the results depended on the average sea level pressure at 65° S and hence on seasonality. As noted previously, the regime transition described in the schematic in our Figure 1 was determined based on 500 hPa geopotential height Z_g^{500hPa} data and therefore was above the high Antarctic interior and its complexities. In addition, the NNR1 and BAS SAM indexes were correlated at 0.83 between 1970 and 1979, increasing to 0.881 in the region from 45° W to 180° E, where the BAS SAM was defined. Hence, not only is the node of the hemispheric wave-3 blocking pattern in the Australian sector well observed by the Australian radiosonde and rawinsonde network but there is also a strong correspondence between the associated NNR1 and BAS SAM indices in the decade prior to the regime transition.
- In addition to the points above, we should note that in the Australian region and more broadly in the eastern hemisphere, the signal of regime change is also seen in the 20CR reanalysis version 2 [88]. This reanalysis is based on interpolated monthly sea-surface temperature and sea-ice concentration fields from the Hadley Centre Sea Ice and SST dataset (HadISST), prescribed as boundary conditions, along with surface pressure observations. It produces a reanalysis dataset spanning from 1871 to the present for field assimilation. Freitas et al. (2015) [50] employed ensemble GCM simulations with observed sea surface temperatures (SSTs) and historical time-evolving carbon dioxide (CO₂) concentrations to investigate the interdecadal changes in the jet streams, temperature, Hadley circulation, mean sea level pressure and precipitation for the mean July climate fields of 1949–1968 and 1975–1994, as compared to reanalyzed observations from NNR1 and the 20CR. They found that model simulations with historical time-evolving CO₂ concentrations were more skillful in reproducing the interdecadal changes in the atmosphere. Indeed, based on these discussions, we would reasonably expect that analyses based on NNR1 data at 500 hPa would follow the observations sufficiently closely for the results in Figure 1 to be a reasonable estimate of the time series around 1957 and after 1970. Even considering only reanalyses after 1979, as in [15], the divergence of the two time series is consistent with the timing of the atmospheric regime transition noted previously.
- According to [22] (p. 441), *It is worth noting that the reanalysis product was explicitly not designed to be appropriate for temporal analyses, but rather to be the best representation of the atmosphere at any point in time*. In the analysis that generated our Figure 1, we applied the FEM-BV-VARX machine learning methodology that specifically targets the feature space associated with the daily synoptic weather patterns. The methodology is not a simple trend analysis (see Appendix B), but rather a sophisticated approach that assigns daily 500 hPa anomalies to nonstationary regime states. Once this has been achieved, one can then apply LOWESS fits to the daily affiliation sequence to identify systematic shifts in the frequency of occurrence and persistence of those regime states, along with associated changes in the structure of the regime states. Thus, our analysis is completely consistent with the reanalysis methodology for the best reconstruction of the atmosphere based on available observations per the assimilation cycle length. The

FEM-BV-VARX methodology is robust and has been used to understand atmospheric blocking, not only in the NH [89] and SH [28] but also in the context of the NAO [90] and the 2010 Russian heatwave [91].

In summary, it is our contention that there is great consistency in the synchronous or sequential timing of the regime transitions that we have presented, and although there are uncertainties about the NNR1 and JRA55 reanalysis, the timing of the regime transition is robust.

Appendix B. FEM-BV-VARX Clustering

The finite element–bounded variation–vector auto-regressive with external factors (FEM-BV-VARX) method, as applied to atmospheric reanalyses, has been described in detail elsewhere [15,28,29] and is now well documented [14,92]. Here, we provide only a very brief outline of the method and refer interested readers to the citations provided. The FEM-BV-VARX analysis in the studies presented here is typically applied to anomalies calculated as deviations from the climatological mean but without detrending in order to preserve secular behaviors. The purpose of reducing dimensionality using principal component analysis (PCA) is to restrict the features present in the data, which depends on the selection of fields and how the singular-value decomposition is formulated. To this end, a series of experiments need to be undertaken to ascertain the sensitivity to retained dimensions and how the covariances are constructed.

The general approach is to fit a nonstationary stochastic model to the data and determine the optimal set of time-evolving free model parameters. Let $\mathbf{x}_0, \dots, \mathbf{x}_T \in \Psi \subset \mathbf{R}^n$ be the observed n -dimensional time series with $T + 1$ daily averages in the interval $[0, T]$. Assume that \mathbf{x}_t can be approximated by the time-discrete output of a particular direct mathematical model $F[\mathbf{x}_t, \dots, \mathbf{x}_{t-m\tau}, \theta(t), t] = 0$, where $F(\cdot)$ is the model operator, t is the model time step, $m\tau$ is the memory depth, and $\theta(t) : [0, T] \rightarrow \Omega \subset \mathbf{R}^d$ is the (time-dependent) set of model parameters, with d representing the dimension of a model parameter space. Following the approach in [93], we next define a model distance functional (sometimes referred to as a loss function) $g[\mathbf{x}_t, \theta(t)] : \Psi \times \Omega \rightarrow [0, \infty)$, describing the distance (or loss) between some given \mathbf{x}_t at time t and the output of the model $F(\cdot)$ calculated for a fixed set of parameters $\theta(t)$. For a given observation series $\mathbf{x}_0, \dots, \mathbf{x}_T$ and some fixed functional form $g(\cdot)$, the inverse problem (or the parameter identification problem) can be approached via the solution of the following variational problem:

$$\sum_{t=1}^T g[\mathbf{x}_t, \theta(t)] \rightarrow \min \theta(t) \quad (\text{A1})$$

subject to the constraints given above.

The problem as it stands is ill-posed and requires some assumptions to be made about the temporal dependence of the unknown parameters $\theta(t)$. Following [93,94], we now assume that for any $t \in [0, T]$, the model distance functional $g[\mathbf{x}_t, \theta(t)]$ can be represented as a convex linear combination of $K \geq 1$ stationary model distance functionals, i.e., model functionals, which depend on some constant (time-independent) model parameters $\theta_i \in \Omega$, where $i = 1, \dots, K$, such that

$$g[\mathbf{x}_t, \theta(t)] = \sum_{i=1}^K \gamma_i(t) g(\mathbf{x}_t, \theta_i) \quad (\text{A2})$$

with a convex set of time-dependent model affiliations $\gamma_i(t)$, i.e.,

$$\sum_{i=1}^K \gamma_i(t) = 1, \quad \forall t \in [0, T], \quad (\text{A3})$$

$$\gamma_i(t) \geq 0, \quad \forall t \in [0, T], \quad i = 1, \dots, K \quad (\text{A4})$$

where $\Theta = \theta_1, \dots, \theta_K$. The assumption here is that at any time t , the global time-dependent (or nonstationary) model distance functional $g[\mathbf{x}_t, \theta(t)] : \Psi \times \Omega \rightarrow [0, \infty)$ can be approximated by one of K local time-independent (or stationary) model distance functionals, chosen based on some time-dependent probabilities (or model affiliations) $\Gamma = [\gamma_1(t), \dots, \gamma_K(t)]$.

The FEM-BV-VARX method approximates dynamical processes using a stochastic model of the form:

$$\mathbf{x}_t = \mu_t + \mathbf{A}(t)\phi_1(\mathbf{x}_{t-\tau}, \dots, \mathbf{x}_{t-m\tau}) + \mathbf{B}(t)\phi_2(u_t) + \mathbf{C}(t)\epsilon_t \quad (\text{A5})$$

where $\Theta = (\mu(t), \mathbf{A}(t), \mathbf{B}(t), \mathbf{C}(t))$ is the vector of time-dependent model parameters with mean $\mu(t)$. ϕ_1 is, in general, a nonlinear function connecting present and past observations $(\mathbf{x}_{t-\tau}, \dots, \mathbf{x}_{t-m\tau})$, but here, we take it to be the linear auto-regressive factor model, adopting the perspective of Granger causality (that dwells on stationary auto-regressive models) [7]. $\phi_2(u_t)$ is an external factor function, and $\mathbf{C}(t)$ couples the non-parametric, independent, and identically distributed (i.i.d.) noise process ϵ_t to the analyzed time series (thereby modeling the impact of unresolved subgrid-scale effects). The time dependence of the model parameters Θ is also induced by the influence of the unresolved scales, leading to regime transitions in many realistic systems.

For a given number, K , of clusters and a fixed maximal time lag, m , the method minimizes the distance of the model trajectory (of model metric g) at each time, t , to one of K model clusters. The model metric used is the Euclidean norm, measuring the model error as the squared distance between \mathbf{x}_t and the output of the average model function $g(\mathbf{x}_t, \theta(t)) = \|\mathbf{x}_t - \mu(t) - \mathbf{A}(t)\phi_1(\mathbf{x}_{t-\tau}, \dots, \mathbf{x}_{t-m\tau}) - \mathbf{B}(t)\phi_2[u(t)]\|_2^2$ (see [94] for details). We explicitly compare the results for time lags corresponding to Bernoulli (random memoryless: lag 0), Markovian (dependent only on the prior timestep: lag 1), and non-Markovian (long-term memory effects; here, we consider memory out to 4 days: lags 2–4). The model affiliation sequence

$$\Gamma = \gamma_1(t), \gamma_2(t), \dots, \gamma_K(t) \quad (\text{A6})$$

represents the probability of time spent in each cluster state. The time-dependent vector $\Gamma = (\gamma_1(t), \dots, \gamma_K(t))$ contains the probabilities for an observation x_t at time t to be described/explained by an output of a vector auto-regressive external factor model (VARX) with constant (time-independent) model parameters θ_i . Γ and $\Theta = \theta_1, \dots, \theta_K$ are jointly obtained from the numerical optimization given by Equation (A7). The method treats the clustering of nonstationary multidimensional data $\mathbf{x}_t \in \mathbf{R}^d$ as a minimization problem:

$$L(\Theta, \Gamma) = \sum_{t=0}^T \sum_{i=1}^K \gamma_i(t) g(\mathbf{x}_t, u_t, \theta_i) \rightarrow \min(\Gamma, \Theta) \quad (\text{A7})$$

subject to convexity constraints $\sum_{i=1}^K \gamma_i(t) = 1, \forall t \in [0, T]$ and $\gamma_i(t) \geq 0, \forall t \in [0, T]$, where $i = 1, \dots, K$.

The number of different spatio-temporal regimes/clusters, K , along with the model parameters to be chosen within these regimes (such as the memory depth and the number of PCs) and the indicator functions $\gamma_k(\cdot)$ signaling activation of the respective model regimes, are all determined simultaneously in a global optimization procedure. This yields a judicious compromise between low residuals in reproducing the data of a training set on the one hand, and the demand for the smallest possible overall number of free parameters of the complete model on the other. The resulting FEM-BV framework is essentially non-parametric and parameter-free, apart from the overall number of optimization repetitions (annealing steps) with different randomly chosen initial values Γ or Θ for parameter optimization. Increasing this number reduces the probability of becoming trapped in one of the local minima of L (for $N_C > 0$) while simultaneously linearly increasing the number of computations. Therefore, the number of annealing steps should be chosen carefully, depending on the available computational resources and the size of the data to be analyzed.

The optimization problem is now solved with a finite element approach (see [92,93,95] for more information and a detailed description of the algorithm) using the principal components of the EOFs, as described in [67]. The persistency constraint C bounds the persistency of the function γ_i via the norm

$$|\gamma_i|_{BV(0,T)} = \sum_{t=0}^{T-1} |\gamma_i(t+1) - \gamma_i(t)| = \|D\gamma_i^\dagger\|_1 \leq C, \quad (\text{A8})$$

$$D = \begin{bmatrix} -1 & 1 & \dots & 0 \\ 0 & -1 & \dots & 0 \\ \dots & \dots & \dots & \dots \\ 0 & \dots & -1 & 1 \end{bmatrix},$$

where $i = 1, \dots, K$, the scalar persistence parameter C measures the maximal number of transitions between the local model i and all other models in the time interval $(0, T)$, $\gamma_i = [\gamma_i(1), \dots, \gamma_i(T)] \in \mathbf{R}^T$, \dagger is the transposition operation, and $\|\cdot\|_1$ is the 1-norm.

In the context of nonstationary inference, it is appropriate to use the AIC to determine the right order parameters of the VARX model, i.e., the memory depth m , the number of clusters K , and the optimal BV persistency C [93]. To select the proper order parameters (and the optimal functional for external factors $\phi_2[u_t]$ in Equation (A5)) for a given persistency parameter value (Equation (18) [94], the AIC is defined as follows (for a complete description of the persistency parameter formulation, see section 2d in [94]):

$$AIC = -2 \log L_{max} + 2M, \quad (\text{A9})$$

where L_{max} is the maximum log-likelihood achievable by the model and M is the number of free parameters. The lowest AIC is preferred. It should, however, be appreciated that the AIC can only be applied to discriminate between models of a given dimension. Thus, the AIC can only determine the optimal choice of model parameters (including penalizing for ill-conditioning and overfitting) for a given class of stochastic models with the same fixed number of PCs (dimensions) but whose retained memory information may vary. Therefore, it follows that information-theoretic methods cannot discriminate between models whose parameters have different dimensions, i.e., different retained numbers of PCs.

A key output of the FEM-BV-VARX method is the posterior model affiliation sequence (or Viterbi path), which describes the most likely cluster state, i , of the system at each time. From the Viterbi path, one can construct composites by averaging the anomalous data instances \mathbf{x}_t over all times when the system is in each of the respective regime's states corresponding to the cluster states $i = 1, \dots, K$. Composites of the original data show the spatial structure of each (metastable) cluster state. The Viterbi path also enables the depiction of how long the system remains in each cluster state as it transitions, facilitating the identification of secular trends in each of the regime states. The resulting optimal Viterbi path provides a natural method for generating the climatology of a particular cluster state sequence. Cluster states are constructed by first assigning a model affiliation to each data point in the time series of anomalies according to the Viterbi path or model affiliation sequence Γ . Then, all anomalies for each given cluster state assignment are averaged. The averaged state is the composite or metastable cluster state.

References

1. Dijkstra, H.A. Numerical bifurcation methods applied to climate models: Analysis beyond simulation. *Nonlinear Processes Geophys.* **2019**, *26*, 359–369. [CrossRef]
2. Lenton, T.M.; Rockström, J.; Gaffney, O.; Rahmstorf, S.; Richardson, K.; Steffen, W.; Schellnhuber, H.J. Climate tipping points—Too risky to bet against. *Nature* **2019**, *575*, 592–595. [CrossRef] [PubMed]
3. Yan, P.; Feng, G.; Hou, W.; Yang, P. A method for predicting the uncompleted climate transition process. *Nonlinear Processes Geophys.* **2020**, *27*, 489–500. [CrossRef]
4. Kypke, K.L.; Langford, W.F.; Willms, A.R. Anthropocene climate bifurcation. *Nonlinear Processes Geophys.* **2020**, *27*, 391–409. [CrossRef]

5. Australian Academy of Science. *The Risks to Australia of a 3 °C Warmer World*; Australian Academy of Science: Canberra, Australia, 2021.
6. Frederiksen, J.S.; Osbrough, S.L. Tipping Points and Changes in Australian Climate and Extremes. *Climate* **2022**, *10*, 73. [[CrossRef](#)]
7. Granger, C.W.J. Investigating Causal Relations by Econometric Models and Cross-spectral Methods. *Econometrica* **1969**, *37*, 424–438. [[CrossRef](#)]
8. Sugihara, G.; May, R.; Hao, Y.; Chih-hao, H.; Deyle, E. Detecting Causality in Complex Ecosystems. *Science* **1969**, *338*, 496–500. [[CrossRef](#)]
9. Horenko, I. Cheap robust learning of data anomalies with analytically solvable entropic outlier sparsification. *Proc. Natl. Acad. Sci. USA* **2022**, *119*, e2119659119. [[CrossRef](#)]
10. Horenko, I. On a Scalable Entropic Breaching of the Overfitting Barrier for Small Data Problems in Machine Learning. *Neural Comput.* **2020**, *132*, 1563–1579. [[CrossRef](#)]
11. Vecchi, E.; Pospíšil, L.; Albrecht, S.; O’Kane, T.J.; Horenko, I. eSPA+: Scalable Entropy-Optimal Machine Learning Classification for Small Data Problems. *Neural Comput.* **2022**, *119*, e2119659119. [[CrossRef](#)]
12. Horenko, I.; Vecchi, E.; Kardoš, J.; Wächter, A.; Schenk, O.; O’Kane, T.J.; Gagliardini, P.; Gerber, S. On cheap entropy-sparsified regression learning. *Proc. Natl. Acad. Sci. USA* **2022**, *120*, e221497212. [[CrossRef](#)] [[PubMed](#)]
13. Horenko, I. Nonstationarity in multifactor models of discrete jump processes, memory and application to cloud modeling. *J. Atmos. Sci.* **2011**, *68*, 1493–1506. [[CrossRef](#)]
14. Metzner, P.; Putzig, L.; Horenko, I. Analysis of persistent nonstationary time series and applications. *Commun. Appl. Math. Comp. Sci.* **2012**, *7*, 175–229. [[CrossRef](#)]
15. O’Kane, T.J.; Risbey, J.S.; Franzke, C.L.E.; Horenko, I.; Monselesan, D.P. Changes in the Metastability of the Midlatitude Southern Hemisphere Circulation and the Utility of Nonstationary Cluster Analysis and Split-Flow Blocking Indices as Diagnostic Tools. *J. Atmos. Sci.* **2013**, *70*, 824–842. [[CrossRef](#)]
16. Vercauteren, N.; Klein, R. A clustering method to characterize intermittent bursts of turbulence and interaction with submesoscale motions in the stable boundary layer. *J. Atmos. Sci.* **2014**, *72*, 1504–1517. [[CrossRef](#)]
17. O’Kane, T.J.; Sandery, P.A.; Kitsios, V.; Sakov, P.; Chamberlain, M.A.; Collier, M.A.; Fiedler, R.; Moore, T.S.; Chapman, C.C.; Sloyan, B.M.; et al. CAFE60v1: A 60-Year Large Ensemble Climate Reanalysis. Part I: System Design, Model Configuration, and Data Assimilation. *J. Clim.* **2021**, *34*, 5153–5169. [[CrossRef](#)]
18. Kistler, R.; Kalnay, E.; Collins, W.; Saha, S.; White, G.; Woollen, J.; Chelliah, M.; Ebisuzaki, W.; Kanamitsu, M.; Kousky, V.; et al. The NCEP-NCAR 50-year reanalysis: Monthly means CD-ROM and documentation. *Bull. Am. Meteor. Soc.* **2001**, *82*, 247–267. [[CrossRef](#)]
19. Bengtsson, L.; Hagemann, S.; Hodges, K.I. Can climate trends be calculated from reanalysis data? *J. Geophys. Res. Atmos.* **2004**, *109*, D11. [[CrossRef](#)]
20. Hines, K.M.; Bromwich, D.H.; Marshall, G.J. Artificial Surface Pressure Trends in the NCEP/NCAR Reanalysis over the Southern Ocean and Antarctica. *J. Clim.* **2000**, *13*, 3940–3952. [[CrossRef](#)]
21. Marshall, G.J. Trends in the Southern Annular Mode from Observations and Reanalyses. *J. Clim.* **2003**, *16*, 4134–4143. [[CrossRef](#)]
22. Kalnay, E.; Reynolds, R.; Jenne, R.; Joseph, D. The NCEP/NCAR 40-Year Re-analysis Project. *Bull. Am. Meteor. Soc.* **1996**, *77*, 437–471. [[CrossRef](#)]
23. Marques, R.F.C.; Rao, V.B. Interannual variations of blocking in the Southern Hemisphere. *J. Geophys. Res.* **2000**, *105*, 4625–4636. [[CrossRef](#)]
24. Frederiksen, J.S.; Frederiksen, C.S. Interdecadal changes in southern hemisphere winter storm track modes. *Tellus A* **2007**, *59*, 599–617. [[CrossRef](#)]
25. Wiedenmann, J.M.; Lupo, A.R.; Mokhov, I.I.; Tikhonova, E.A. The climatology of blocking anti-cyclones for the Northern and Southern Hemispheres: Block Intensity as a diagnostic. *J. Clim.* **2002**, *15*, 3459–3473. [[CrossRef](#)]
26. van Loon, H.; Jenne, R.L. The zonal harmonic standing waves in the Southern Hemisphere. *J. Geophys. Res.* **2002**, *77*, 992–1003. [[CrossRef](#)]
27. Trenberth, K.E.; Mo, K.C. Blocking in the Southern Hemisphere. *Mon. Weather Rev.* **2002**, *113*, 3–21. [[CrossRef](#)]
28. Franzke, C.L.E.; O’Kane, T.J.; Monselesan, D.P.; Risbey, J.S.; Horenko, I. Systematic attribution of observed Southern Hemispheric circulation trends to external forcing and internal variability. *Nonlinear Processes Geophys.* **2015**, *2*, 675–707. [[CrossRef](#)]
29. O’Kane, T.J.; Risbey, J.S.; Monselesan, D.P.; Horenko, I.; Franzke, C.L.E. On the dynamics of persistent states and their secular trends in the waveguides of the Southern Hemisphere troposphere. *Clim. Dyn.* **2016**, *46*, 3567–3597. [[CrossRef](#)]
30. Frederiksen, J.S.; Frederiksen, C.S. Decadal Changes in Southern Hemisphere Winter Cyclogenesis. In *CSIRO Marine and Atmospheric Research Paper*; CSIRO: Melbourne, Australia, 2005; Volume 2, p. 29. Available online: http://www.cmar.csiro.au/eprint/open/frederiksenjs_2005b.pdf (accessed on 30 April 2024).
31. Frederiksen, J.S.; Frederiksen, C.S. Twentieth Century Winter Changes in Southern Hemisphere Synoptic Weather Modes. *Adv. Meteorol.* **2011**, *2011*, 353829. [[CrossRef](#)]
32. Corti, S.; Molteni, F.; Palmer, T.N. Signature of recent climate change in frequencies of natural atmospheric circulation regimes. *Nature* **1999**, *398*, 799–802. [[CrossRef](#)]
33. Kobayashi, S.; Ota, Y.; Harada, Y.; Ebata, A.; Moriya, M.; Onoda, H.; Onogi, K.; Kamahori, H.; Kobayashi, C.; Endo, H.; et al. The JRA-55 Reanalysis: General Specifications and Basic Characteristics. *J. Meteorol. Soc. Jpn. Ser. II* **2015**, *93*, 5–48. [[CrossRef](#)]

34. O’Kane, T.J.; Monselesan, D.P.; Risbey, J.S.; Horenko, I.; Franzke, C.L.E. On memory, dimension, and atmospheric teleconnections. *Math. Clim. Weather Forecast.* **2017**, *3*, 1–27. [[CrossRef](#)]
35. Arblaster, J.M.; Meehl, G.A. Contributions of External Forcings to Southern Annular Mode Trends. *J. Clim.* **2006**, *19*, 2896–2905. [[CrossRef](#)]
36. Turner, J.; Comiso, J.C.; Marshall, G.J.; Lachlan-Cope, T.A.; Bracegirdle, T.; Maksym, T. Non-annular atmospheric circulation change induced by stratospheric ozone depletion and its role in the recent increase of Antarctic sea ice extent. *Geophys. Res. Lett.* **2009**, *36*, L08502. [[CrossRef](#)]
37. Son, S.W.; Gerber, E.P.; Perlwitz, J.; Polvani, L.M.; Gillett, N.P.; Seo, K.H.; Eyring, V.; Shepherd, T.G.; Waugh, D.; Akiyoshi, H.; et al. Impact of stratospheric ozone on Southern Hemisphere circulation change: A multimodel assessment. *J. Geophys. Res.* **1999**, *115*, D00M07. [[CrossRef](#)]
38. Previdi, M.; Polvani, L.M. Climate system response to stratospheric ozone depletion and recovery. *Q. J. Roy. Meteorol. Soc.* **2014**, *140*, 2401–2419. [[CrossRef](#)]
39. Barnes, E.A.; Barnes, N.W.; Polvani, L.M. Delayed Southern Hemisphere climate change induced by stratospheric ozone recovery, as projected by the CMIP5 models. *J. Clim.* **2013**, *276*, 852–867. [[CrossRef](#)]
40. Frederiksen, C.S.; Frederiksen, J.S.; Sisson, J.; Osbrough, S.L. Trends and projections of Southern Hemisphere baroclinicity: The role of external forcing and impact on Australian rainfall. *Clim. Dyn.* **2017**, *48*, 3261–3282. [[CrossRef](#)]
41. Trenberth, K.E. Storm tracks in the Southern Hemisphere. *J. Atmos. Sci.* **1991**, *48*, 2159–2178. [[CrossRef](#)]
42. Steele, L.P.; Krummel, P.B.; Langenfelds, R.L. Atmospheric CO₂ Concentrations from Sites in the CSIRO Atmospheric Research GASLAB Air Sampling Network (August 2007 Version). In *Trends: A Compendium of Data on Global Change; Carbon Dioxide Information Analysis Center, Oak Ridge National Laboratory, US Department of Energy: Oak Ridge, TN, USA*, 2007.
43. Skeie, R.B.; Berntsen, T.K.; Myhre, G.; Tanaka, K.; Kvalevåg, M.M.; Hoyle, C.R. Anthropogenic radiative forcing time series from pre-industrial times until 2010. *Atmos. Chem. Phys.* **2011**, *11*, 11827–11857. [[CrossRef](#)]
44. Bourassa, A.E. Large volcanic aerosol load in the stratosphere linked to Asian monsoon transport. *Science* **2011**, *337*, 78–82. [[CrossRef](#)] [[PubMed](#)]
45. Fröhlich, C. Observations of irradiance variations. *Space Sci. Rev.* **2000**, *94*, 15–24. [[CrossRef](#)]
46. Roscoe, H.K.; Haigh, J.D. Influences of ozone depletion, the solar cycle and the QBO on the Southern Annular Mode. *Q. J. Roy. Meteorol. Soc.* **2007**, *133*, 1855–1864. [[CrossRef](#)]
47. Parzen, E.; Tanabe, K.; Kitagawa, G. (Eds.) *Information Theory and an Extension of the Maximum Likelihood Principle: Selected Papers of Hirotugu Akaike*; Springer: Berlin/Heidelberg, Germany, 1988.
48. Cowtan, K.; Way, R.G. Coverage bias in the HadCRUT4 temperature series and its impact on recent temperature trends. *Q. J. R. Meteorol. Soc.* **2014**, *140*, 1935–1944. [[CrossRef](#)]
49. Lee, S.; Feldstein, S.B. Detecting Ozone- and Greenhouse Gas-Driven Wind Trends with Observational Data. *Science* **2013**, *339*, 563–567. [[CrossRef](#)]
50. Freitas, A.C.V.; Frederiksen, J.S.; Whelan, J.; O’Kane, T.J.; Ambrizzi, T. Observed and simulated inter-decadal changes in the structure of Southern Hemisphere large-scale circulation. *Clim. Dyn.* **2015**, *45*, 2993–3017. [[CrossRef](#)]
51. Saji, N.H.; Goswami, B.N.; Vinayachandran, P.N.; Yamagata, T. A dipole mode in the tropical Indian Ocean. *Nature* **1999**, *401*, 360–363. [[CrossRef](#)]
52. Mo, K.C. Relationships between Low-Frequency Variability in the Southern Hemisphere and Sea Surface Temperature Anomalies. *J. Clim.* **2000**, *13*, 3599–3610. [[CrossRef](#)]
53. Troup, A.J. The ‘Southern Oscillation’. *Q. J. R. Met. Soc.* **1965**, *91*, 490–506. [[CrossRef](#)]
54. Gallant, A.J.E.; Hennessy, K.J.; Risbey, J. Trends in rainfall indices for six Australian regions: 1910–2005. *Aust. Meteorol. Mag.* **2007**, *56*, 223–239.
55. Hendon, H.; Thompson, D.; Wheeler, M. Australian Rainfall and Surface Temperature Variations Associated with the Southern Hemisphere Annular Mode. *J. Clim.* **2007**, *20*, 2452–2467. [[CrossRef](#)]
56. Ummenhofer, C.C.; England, M.H.; McIntosh, P.C.; Meyers, G.A.; Pook, M.J.; Risbey, J.S.; Gupta, A.S.; Taschetto, A.S. What causes southeast Australia’s worst droughts? *Geophys. Res. Lett.* **2009**, *36*, L04706. [[CrossRef](#)]
57. Cai, W.; Cowan, T.; Sullivan, A. Recent unprecedented skewness towards positive Indian Ocean Dipole occurrences and its impact on Australian rainfall. *Geophys. Res. Lett.* **2009**, *36*, L11705. [[CrossRef](#)]
58. Frederiksen, C.S.; Grainger, S. The role of external forcing in prolonged trends in Australian rainfall. *Clim. Dyn.* **2015**, *45*, 2455–2468. [[CrossRef](#)]
59. Dey, R.; Lewis, S.; Abram, N.; Arblaster, J. A review of past and projected changes in Australia’s rainfall. *Wiley Interdiscip. Rev. Clim. Change* **2015**, *10*, e557. [[CrossRef](#)]
60. Phillips, N.A. Energy Transformations and Meridional Circulations associated with simple Baroclinic Waves in a two-level, Quasi-geostrophic Model. *Tellus* **2002**, *6*, 273–286. [[CrossRef](#)]
61. Frederiksen, C.S.; Frederiksen, J.S. A theoretical model of Australian Northwest cloud band disturbances and Southern Hemisphere storm tracks: The role of SSTs. *J. Atmos. Sci.* **1996**, *49*, 1410–1432. [[CrossRef](#)]
62. Risbey, J.S.; McIntosh, P.C.; Pook, M.J. Synoptic components of rainfall variability and trends in southeast Australia. *Int. J. Climatol.* **2013**, *33*, 2459–2472. [[CrossRef](#)]

63. O’Kane, T.J.; Matear, R.J.; Chamberlain, M.A.; Oke, P.R. ENSO regimes and the late 1970s climate shift: The role of synoptic weather and South Pacific ocean spiciness. *J. Comp. Phys.* **2014**, *271*, 19–38. [[CrossRef](#)]
64. O’Kane, T.J.; Matear, R.J.; Chamberlain, M.A.; Risbey, J.S.; Sloyan, B.M.; Horenko, I. Decadal variability in an OGCM Southern Ocean: Intrinsic modes, forced modes and metastable states. *Ocean. Model.* **2013**, *69*, 1–21. [[CrossRef](#)]
65. Lou, J.; O’Kane, T.J.; Holbrook, N.J. A Linear Inverse Model of Tropical and South Pacific Seasonal Predictability. *J. Clim.* **2020**, *33*, 4537–4554. [[CrossRef](#)]
66. O’Kane, T.J.; Sandery, P.A.; Kitsios, V.; Sakov, P.; Chamberlain, M.A.; Squire, D.T.; Collier, M.A.; Chapman, C.C.; Fiedler, R.; Harries, D.; et al. CAFE60v1: A 60-Year Large Ensemble Climate Reanalysis. Part II: Evaluation. *J. Clim.* **2021**, *34*, 5171–5194. [[CrossRef](#)]
67. Horenko, I. On Simultaneous Data-Based Dimension Reduction and Hidden Phase Identification. *J. Atmos. Sci.* **2008**, *65*, 1941–1954. [[CrossRef](#)]
68. O’Kane, T.J.; Matear, R.J.; Chamberlain, M.A.; Oliver, E.C.J.; Holbrook, N.J. Storm tracks in the Southern Hemisphere subtropical oceans. *J. Geophys. Res. Ocean.* **2014**, *119*, 6078–6100. [[CrossRef](#)]
69. Chapman, C.C.; Sloyan, B.M.; O’Kane, T.J.; Chamberlain, M.A. Interannual Subtropical Indian Ocean Variability due to Long Baroclinic Planetary Waves. *J. Geophys. Res. Ocean.* **2020**, *33*, 6765–6791. [[CrossRef](#)]
70. Sloyan, B.M.; O’Kane, T.J. Drivers of decadal variability in the Tasman Sea. *J. Geophys. Res. Ocean.* **2015**, *120*, 1–18. [[CrossRef](#)]
71. O’Kane, T.J.; Monselesan, D.P.; Risbey, J.S. A multiscale re-examination of the Pacific South American pattern. *Mon. Weather Rev.* **2017**, *145*, 379–402. [[CrossRef](#)]
72. Lou, J.; O’Kane, T.J.; Holbrook, N.J. Linking the atmospheric Pacific-South American mode with oceanic variability and predictability. *Commun. Earth Environ.* **2021**, *2*, 223. [[CrossRef](#)]
73. Griffies, S. Elements of MOM4p1. In *GFDL Ocean Group Technical Report 6*; NOAA/Geophysical Fluid Dynamics Laboratory: Princeton, NJ, USA, 2009.
74. Nonaka, M.; Sasaki, H. Formation mechanism for isopycnal temperature-salinity anomalies propagating from the eastern South Pacific to the equatorial region. *J. Clim.* **2007**, *20*, 1305–1315. [[CrossRef](#)]
75. Kolodziejczyk, N.; Gaillard, F. Variability of the heat and salt budget in the subtropical southeastern Pacific mixed layer between 2004 and 2010: Spice injection mechanism. *J. Phys. Oceanogr.* **2013**, *43*, 1880–1898. [[CrossRef](#)]
76. Munk, W. Internal waves and small scale processes. In *Evolution of Physical Oceanography*; MIT Press: Cambridge, MA, USA, 1981.
77. Tailleux, A.; Lazar, A.; Reason, C. Physics and dynamics of density-compensated temperature and salinity anomalies. Part 1: Theory. *J. Phys. Oceanogr.* **2005**, *35*, 849–864. [[CrossRef](#)]
78. Giese, B.; Urizar, S.; Fuckar, N. Southern hemisphere origins of the 1976 climate shift. *Geophys. Res. Lett.* **2002**, *29*, 1014. [[CrossRef](#)]
79. Harries, D.; O’Kane, T.J. Dynamic Bayesian networks for evaluation of Granger causal relationships in climate reanalyses. *J. Adv. Model. Earth Syst.* **2021**, *13*, e2020MS0024420. [[CrossRef](#)]
80. Frederiksen, C.S.; Frederiksen, J.S.; Sisson, J.; Osbrough, S.L. Changes and Projections in Australian Winter Rainfall and Circulation: Anthropogenic Forcing and Internal Variability. *Int. J. Clim. Change* **2011**, *2*, 143–162. [[CrossRef](#)]
81. Grainger, S.; Frederiksen, C.S.; Zheng, X. Projections of Southern Hemisphere atmospheric circulation interannual variability. *Clim. Dyn.* **2017**, *48*, 1187–1211. [[CrossRef](#)]
82. Johnson, G.C.; Hosoda, S.; Jayne, S.R.; Oke, P.R.; Riser, S.C.; Roemmich, D.; Suga, T.; Thierry, V.; Wijffels, S.E.; Xu, J. Argo-Two Decades: Global Oceanography, Revolutionized. *Annu. Rev. Mar. Sci.* **2022**, *14*, 379–403. [[CrossRef](#)]
83. Franzke, C.; Horenko, I.; Majda, A.J.; Klein, R. Systematic Metastable Atmospheric Regime Identification in an AGCM. *J. Atmos. Sci.* **2009**, *66*, 1997–2012. [[CrossRef](#)]
84. Gwyther, D.E.; O’Kane, T.J.; Galton-Fenzi, B.K.; Monselesan, D.P.; Greenbaum, J.S. Intrinsic processes drive variability in basal melting of the Totten Glacier Ice Shelf. *Nat. Commun.* **2018**, *9*, 3141. [[CrossRef](#)]
85. Hertzog, A.; Basdevant, C.; Vial, F. An assessment of ECMWF and NCEP/NCAR reanalyses in the Southern Hemisphere at the end of the pre-satellite era: Results from the EOLE experiment (1971–1972). *Mon. Weather Rev.* **2004**, *134*, 3367–3383. [[CrossRef](#)]
86. Bromwich, D.; Fogt, R. Strong trends in the skill of the ERA-40 and NCEP-NCAR reanalysis in the high and midlatitudes of the Southern Hemisphere 1958–2001. *J. Clim.* **2004**, *17*, 4603–4619. [[CrossRef](#)]
87. Marshall, G.J. Trends in Antarctic geopotential height and temperature: A comparison between radiosonde and NCEP/NCAR reanalysis data. *J. Clim.* **2002**, *15*, 659–674. [[CrossRef](#)]
88. Compo, G.; Whitaker, J.; Sardeshmukh, P.; Matsui, N.; Allan, R.; Yin, X.; Gleason, B.; Vose, R.; Rutledge, G.; Bessemoulin, P.; et al. The Twentieth Century Reanalysis Project. *Q. J. R. Meteorol. Soc.* **2011**, *137*, 1–28. [[CrossRef](#)]
89. Risbey, J.S.; O’Kane, T.; Monselesan, D.; Franzke, C.; Horenko, I. Metastability of Northern Hemisphere teleconnection modes. *J. Atmos. Sci.* **2015**, *72*, 35–54. [[CrossRef](#)]
90. Quinn, C.; Harries, D.; O’Kane, T. Dynamical analysis of a reduced model for the North Atlantic Oscillation. *J. Atmos. Sci.* **2021**, *78*, 1647–1671. [[CrossRef](#)]
91. Quinn, C.; O’Kane, T.; Harries, D. Systematic calculation of finite-time mixed singular vectors and characterization of error growth for persistent coherent atmospheric disturbances over Eurasia. *Chaos Interdiscip. J. Nonlinear Sci.* **2022**, *32*, 023126. [[CrossRef](#)] [[PubMed](#)]
92. Horenko, I. On robust estimation of low-frequency variability trends in discrete Markovian sequences of atmospheric circulation patterns. *J. Atmos. Sci.* **2009**, *66*, 1941–1954. [[CrossRef](#)]

93. Horenko, I. Finite element approach to clustering of multidimensional time series. *SIAM J. Sci. Comput.* **2010**, *32*, 62–83. [[CrossRef](#)]
94. Horenko, I. On the identification of nonstationary factor models and their application to atmospheric data sets. *J. Atmos. Sci.* **2010**, *67*, 1559–1574. [[CrossRef](#)]
95. Horenko, I. On clustering of non-stationary meteorological time series. *Dyn. Atmos. Ocean.* **2010**, *49*, 164–187. [[CrossRef](#)]

Disclaimer/Publisher’s Note: The statements, opinions and data contained in all publications are solely those of the individual author(s) and contributor(s) and not of MDPI and/or the editor(s). MDPI and/or the editor(s) disclaim responsibility for any injury to people or property resulting from any ideas, methods, instructions or products referred to in the content.